Journal of Asian Earth Sciences 186 (2019) 104062

Contents lists available at ScienceDirect

Journal of Asian Earth Sciences

journal homepage: www.elsevier.com/locate/jseaes

Subduction-driven heterogeneity of the lithospheric mantle beneath the Cathaysia block, South China

Yan Xiao[a,b,*], Hong-Fu Zhang[a,b,c], Ben-Xun Su[b,d,e], Zi Liang[a,b,e], Bin Zhu[a,b,e], Patrick Asamoah Sakyi[f]

[a] State Key Laboratory of Lithospheric Evolution, Institute of Geology and Geophysics, Chinese Academy of Sciences, Beijing 100029, China
[b] Innovation Academy for Earth Science, Chinese Academy of Sciences, Beijing 100029, China
[c] State Key Laboratory of Continental Dynamics, Department of Geology, Northwest University, Xi'an 710069, China
[d] Key Laboratory of Mineral Resources, Institute of Geology and Geophysics, Chinese Academy of Sciences, Beijing 100029, China
[e] University of Chinese Academy of Sciences, Beijing 100049, China
[f] Department of Earth Science, School of Physical and Mathematical Sciences, University of Ghana, PO Box LG 58, Legon-Accra, Ghana

ARTICLE INFO

Keywords:
Li isotopes
Mantle xenolith
Regional heterogeneity
Subduction
The Cathaysia block

ABSTRACT

To evaluate the modification of the lithospheric mantle by the Paleo-Pacific Ocean subduction beneath the Cathaysia block, we report major and trace elements, and Li isotopes of olivine from Niutoushan, Mingxi, Xilong and Jiande peridotite xenoliths in South China. Spoon-shaped, convex-upward and highly LREE-enriched chondrite-normalized REE patterns of clinopyroxene in the Niutoushan, Mingxi and Xilong xenoliths reflect the interplay between partial melting and subsequent enrichment by metasomatism. Lithium isotope systematics indicate that at least two different metasomatic events affected these peridotites. High Li concentrations in clinopyroxene (up to 59.1 ppm) are ascribed to diffusive Li influx from silicate melts. Olivine grains with lower diffusivity of Li have much higher Li concentrations (0.56–9.76 ppm) and lighter δ^7Li values (−52.75 to +10.49‰) than those in the Jiande and other peridotite xenoliths worldwide, showing a prominent carbonatite-metasomatic signature occurring before silicate metasomatism. In addition, increasing Li concentrations of olivine and clinopyroxene with increasing distance from the present subduction trench is consistent with those of low δ^{26}Mg basalts in South China, indicating that the metasomatic agent was related to the westward subduction of the Paleo-Pacific slab. The Jiande lherzolite xenoliths further away from the trench show 'mantle-like' Li features and may represent upwelling asthenospheric materials accreted to the continent. Therefore, both types of metasomatism as well as upwelling asthenosphere could have played an important role in the modification of the chemical composition of the mantle beneath the Cathaysia block.

1. Introduction

Asthenosphere-lithosphere and mantle-crust interactions can modify and even replace refractory sub-continental lithospheric mantle by the flux of fertile materials (Menzies et al., 1993; Griffin et al., 1998; O'Reilly et al., 2001). The eastern North China Craton (NCC) is the best example of lithospheric modification (Carlson et al., 2005), that experienced widespread tectonothermal reactivation and consequent large-scale lithospheric thinning and transformation since the late Mesozoic (e.g., Fan and Menzies, 1992; Griffin et al., 1998; Menzies and Xu, 1998; Fan et al., 2000; Xu, 2001; Zheng et al., 2001; Zhang et al., 2003; Yang et al., 2018). The mechanism of the lithospheric transformation has been attributed to the subduction of surrounding plates, namely; the Paleo-Asian Ocean to the north, the Yangtze plate to the south, and the Pacific Ocean to the east (Li et al., 1993; Xiao et al., 2003; Wu et al., 2005; Zhu and Zheng, 2009; Windley et al., 2010). These complex subduction events occurring in the NCC make it difficult to determine the spatial and temporal contribution of one single specific slab. In fact, lithospheric modification has also been proposed for other parts of eastern China such as the Cathaysia block that overlies the westward subduction zone of the Pacific Plate since the mid-Permian (Fan and Hooper, 1989; Qi et al., 1995; Xu et al., 2000, 2003; Zou et al., 2000; Fan et al., 2000; Yu et al., 2003; Zheng et al., 2004; Zhang et al., 2007; Huang and Xu, 2010; Yu et al., 2011; Liu et al., 2012, 2017, 2016). Therefore, the geochemical imprints of the lithospheric mantle beneath the Cathaysia block may provide important constraints on the

* Corresponding author at: State Key Laboratory of Lithospheric Evolution, Institute of Geology and Geophysics, Chinese Academy of Sciences, Beijing 100029, China.
E-mail address: xiaoyan@mail.iggcas.ac.cn (Y. Xiao).

https://doi.org/10.1016/j.jseaes.2019.104062
Received 16 May 2019; Received in revised form 18 September 2019; Accepted 1 October 2019
Available online 03 October 2019
1367-9120/

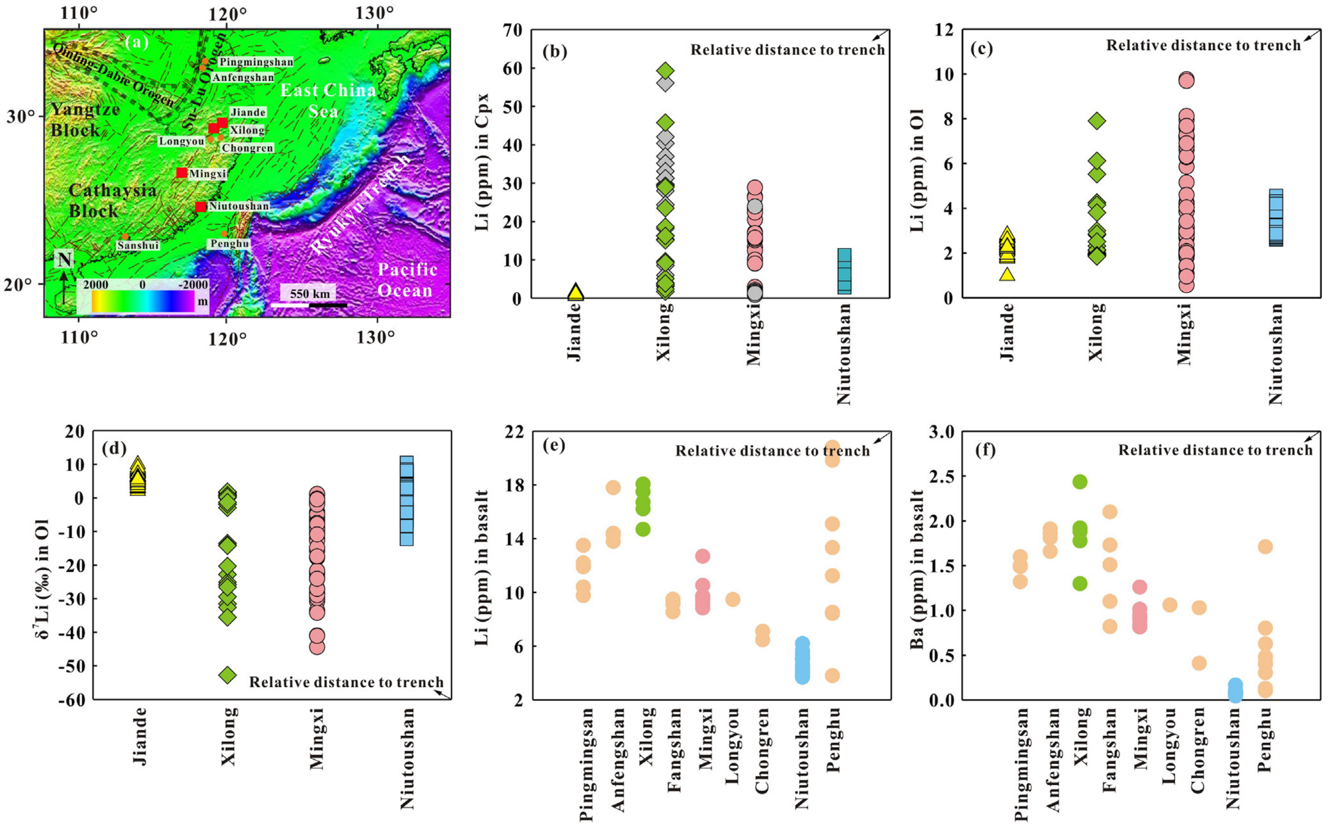

Fig. 1. (a), Geographic map showing major tectonic units in South China (modified after Su et al., 2017). (b–d), Li content and isotopic variations of clinopyroxene and olivine in the peridotites with their relative perpendicular distance to the Pacific subduction trench. (e–f), Li and Ba concentrations variation in basaltic rocks from South China with their relative perpendicular distance to the Pacific subduction trench. The Li concentration and isotopic composition data of clinopyroxene and olivine in the peridotites from the Jiande, Xilong and Mingxi localities are from Lu et al. (2015), Liu et al. (2017) and Xiao et al. (2017). The Li and Ba data of basalts from South China are from Huang et al. (2017) and Su et al. (2017).

timescale of the survival of subducted oceanic slabs.

Lithium (Li) is a moderately incompatible and alkali metal element, possessing two stable isotopes (^{6}Li and ^{7}Li) with ~16% relative mass difference (Chan et al., 1992). At mantle condition, no significant Li isotopic fractionation is considered to occur during partial melting and fractional crystallization (Tomascak et al., 1999; Seitz et al., 2004; Schuessler et al., 2009; Xiao et al., 2017), even though Li isotope systematics could well preserve mantle metasomatic characteristics and discriminate silicate and carbonatite metasomatic agents (Seitz and Woodland, 2000; Su et al., 2014, 2018). In addition, Li is fluid-mobile and concentrated in crustal materials (~18 ppm) compared to mantle domains (< 2 ppm) (Jagoutz et al., 1979; Ryan and Langmuir, 1987; Teng et al., 2008). At subduction zones, Li tend to enter fluids released by slab dehydration and modified mantle wedge (Marschall et al., 2007; Sobolev et al., 2007; Pogge von Strandmann et al., 2011; Xiao et al., 2011). Due to higher affinity of ^{7}Li for fluids than ^{6}Li (Chan and Edmond, 1988; Chan et al., 1992), forearc mantle is thought to be a ^{7}Li-rich reservoir (Benton et al., 2004; Agostini et al., 2008). Furthermore, the progressive shifts toward very negative δ^{7}Li value correlate inversely with distance from the trench as evidenced by subduction zone volcanism and back-arc shield volcano (Moriguti and Nakamura, 1998; Magna et al., 2006). Thus, the Li isotopic system could provide insight into the mantle regimes modified by slab-derived components.

Here, we present major and trace element data, and in-situ Li concentrations and δ^{7}Li values of minerals from peridotite xenoliths entrained in Cenozoic Niutoushan, Mingxi, Xilong and Jiande basalts from the Cathaysia block. The study is aimed at investigating the temporal and spatial Li isotope variation in the sub-lithospheric mantle beneath the Cathaysia block, and to further assess the effect of the subducted Pacific slab on lithospheric heterogeneity beneath the Cathaysia block.

2. Geological setting

Continued westward subduction of the Pacific plate underneath the east Asian continental margin induced the tectonic extension, deep fault development, lithospheric thinning, magmatism and mineralization in East Asia (Zhu et al., 2012; Xu and Zheng, 2017). The South China block, consisting of the Yangtze block to the northwest and the Cathaysia block to the southeast, is a major continental block in East Asia (Fig. 1a). The exposed basement in the Yangtze block is dominantly Proterozoic with scattered Archean outcrops (Qiu et al., 2000). The Cathaysia block is mainly composed of late Neoproterozoic and Phanerozoic sedimentary and igneous rocks with minor exposures of Paleo- and Meso-Proterozoic basement rocks (Liu et al., 2009; Yu et al., 2010; Xia et al., 2012). The Cathaysia block has been considered to be an active continental margin since the mid-Permian (Li and Li, 2007). Along this margin, Mesozoic-Cenozoic volcanic eruptions are developed and dominated by basalts (Fig. 1a; Zhou and Armstrong, 1982; Fan and Hooper, 1991; Zou et al., 2000; Zhu et al., 2012). From east to west, three NE-SW trending volcanic belts occurred in Guangdong, Fujian, and Zhejiang provinces, which are associated with three lithospheric faults (Zou et al., 2000). Most of these basalts contain abundant crustal and mantle xenoliths, which provide a window into the deep lithosphere (Zhang and Cong, 1987). Samples selected for Li isotope analysis in this study are peridotite xenoliths from the Niutoushan, Mingxi, Xilong and Jiande basalts in the Cathaysia block (Fig. 1a; Ho et al., 2003; Hao et al., 2014; Lu et al., 2015; Liu et al., 2017). The Niutoushan basalts in southeastern Fujian Province are within the Changle-Nanao fault of the southeastern coastal area and contain only spinel peridotites (16.6–19.2 Ma; Xu et al., 2000; Yu et al., 2011). The Mingxi (0.9–2.2 Ma) and Xilong (23.7–26.4 Ma) basalts in northwest Fujian

Table 1
Mineral major elements of Niutoushan, Mingxi and Xilong peridotites from the Cathaysia block.

Sample	NTS12-03				NTS12-06				NTS12-7				NTS12-08				NTS12-09			
Rock Type	Spl lherzolite				Spl lherzolite				Spl lherzolite				Spl lherzolite				Spl lherzolite			
Mineral	Ol[a]	Opx	Cpx	Spl	Ol	Opx	Cpx	Spl	Ol	Opx	Cpx	Spl	Ol	Opx	Cpx	Spl	Ol	Opx	Cpx	Spl
SiO_2	41.0	55.5	53.2	0.00	39.7	55.0	52.5	0.23	40.9	54.5	51.5	0.00	41.1	55.5	52.1	0.02	40.6	54.7	51.6	0.01
TiO_2	0.02	0.16	0.46	0.19	0.00	0.09	0.32	0.13	0.04	0.07	0.53	0.11	0.00	0.14	0.46	0.21	0.03	0.07	0.43	0.06
Al_2O_3	0.03	4.66	6.31	54.7	0.03	4.17	5.42	53.3	0.06	4.52	6.57	54.7	0.03	4.10	5.90	52.5	0.02	4.08	6.19	50.5
Cr_2O_3	0.00	0.38	0.83	11.5	0.02	0.37	0.77	13.2	0.05	0.28	0.76	9.63	0.00	0.34	0.74	12.5	0.05	0.47	0.97	15.0
FeO	10.2	6.60	3.29	12.4	9.49	6.05	2.95	11.7	9.95	6.30	3.16	11.7	9.44	6.29	3.08	12.3	11.28	6.79	3.23	13.9
MnO	0.13	0.13	0.10	0.13	0.14	0.14	0.10	0.13	0.18	0.17	0.12	0.09	0.16	0.15	0.09	0.09	0.14	0.12	0.11	0.10
MgO	47.8	32.9	15.5	20.7	49.2	32.8	15.4	20.5	49.0	33.0	15.0	20.5	49.5	33.3	15.7	20.4	48.4	32.9	15.4	19.1
CaO	0.06	0.76	19.2	0.01	0.06	0.62	20.1	0.03	0.05	0.62	20.7	0.00	0.04	0.72	20.5	0.00	0.09	0.69	21.0	0.01
Na_2O	0.02	0.12	1.66	0.01	0.02	0.07	1.32	0.00	0.00	0.09	1.48	0.00	0.00	0.08	1.43	0.00	0.00	0.05	1.19	0.00
K_2O	0.00	0.00	0.02	0.00	0.01	0.00	0.00	0.00	0.00	0.00	0.00	0.00	0.00	0.00	0.00	0.00	0.01	0.00	0.00	0.02
NiO	0.37	0.10	0.10	0.44	0.37	0.14	0.05	0.33	0.42	0.10	0.05	0.39	0.37	0.08	0.03	0.38	0.32	0.12	0.02	0.35
Total	99.7	101.3	100.7	100.1	99.0	99.5	98.9	99.5	100.7	99.7	99.9	97.2	100.6	100.7	100.1	98.4	100.9	99.9	100.2	99.0
Mg#	89.4	90.0	89.4	75.0	90.3	90.7	90.4	75.8	89.9	90.4	89.6	75.9	90.4	90.5	90.2	74.9	88.5	89.7	89.6	71.2
Cr#				12.4				14.2				7.22				7.80				16.7

Sample	NTS12-10				NTS12-11				NTS12-12				NTS12-13				NTS12-14			
Rock Type	Spl lherzolite				Spl lherzolite				Spl lherzolite				Spl lherzolite				Spl lherzolite			
Mineral	Ol	Opx	Cpx	Spl	Ol	Opx	Cpx	Spl	Ol	Opx	Cpx	Spl	Ol	Opx	Cpx	Spl	Ol	Opx	Cpx	Spl
SiO_2	39.9	54.2	51.7	0.04	41.1	56.0	53.6	0.05	41.3	55.4	51.7	0.01	41.1	55.7	52.7	0.10	41.0	55.0	52.3	0.02
TiO_2	0.01	0.12	0.51	0.13	0.02	0.08	0.20	0.13	0.01	0.22	1.03	0.21	0.02	0.08	0.22	0.19	0.00	0.09	0.45	0.21
Al_2O_3	0.02	4.42	6.06	55.2	0.00	3.80	4.55	49.2	0.00	3.89	6.10	53.4	0.00	3.84	5.49	54.2	0.04	4.45	5.92	54.7
Cr_2O_3	0.01	0.33	0.87	11.0	0.01	0.41	0.78	16.5	0.00	0.38	0.88	12.3	0.03	0.30	0.75	11.4	0.04	0.35	0.83	11.6
FeO	11.3	6.08	3.41	11.3	9.86	6.33	2.93	14.2	8.99	5.54	2.76	11.4	9.67	6.24	3.06	13.7	9.75	6.12	3.24	12.4
MnO	0.14	0.13	0.08	0.11	0.15	0.17	0.09	0.07	0.09	0.15	0.07	0.04	0.16	0.15	0.09	0.06	0.14	0.17	0.09	0.10
MgO	47.1	32.6	14.9	21.3	49.3	32.9	16.3	19.1	49.9	33.4	15.7	20.6	49.6	32.7	15.7	20.1	49.4	32.8	15.4	20.5
CaO	0.03	0.72	20.2	0.01	0.06	0.76	21.5	0.01	0.05	0.73	21.4	0.01	0.05	0.66	20.7	0.03	0.08	0.75	20.0	0.00
Na_2O	0.02	0.12	1.36	0.01	0.00	0.05	0.87	0.01	0.00	0.06	1.19	0.00	0.00	0.10	1.47	0.00	0.00	0.10	1.57	0.01
K_2O	0.01	0.01	0.00	0.00	0.01	0.00	0.00	0.01	0.00	0.00	0.02	0.01	0.00	0.00	0.00	0.00	0.01	0.00	0.00	0.00
NiO	0.35	0.10	0.06	0.38	0.40	0.10	0.05	0.33	0.34	0.11	0.04	0.35	0.39	0.07	0.05	0.41	0.37	0.10	0.04	0.40
Total	99.0	98.8	99.1	99.4	100.8	100.6	100.9	99.6	100.7	99.9	100.9	98.3	101.0	99.9	100.2	100.2	100.8	99.9	99.9	100.1
Mg#	88.2	90.6	88.7	77.2	90.0	90.3	90.9	70.8	90.9	91.5	91.1	76.5	90.2	90.4	90.2	72.5	90.1	90.6	89.6	74.9
Cr#				11.8				18.4				8.86				12.4				12.5

Sample	NTS12-15					NTS12-16				NTS12-17				NTS12-18					NTS12-19				
Rock Type	Spl lherzolite					Spl lherzolite				Spl lherzolite				Spl lherzolite					Spl lherzolite				
Mineral	Ol	Opx	Cpx	Cpx2	Spl	Ol	Opx	Cpx	Spl	Ol	Opx	Cpx	Spl	Ol	Opx	Cpx	Cpx2	Spl	Ol	Opx	Cpx	Cpx2	Spl
SiO_2	39.5	54.8	51.9	51.8	0.00	39.2	53.8	51.4	0.00	39.3	54.4	51.8	0.03	40.6	55.2	51.9	51.2	0.06	40.2	55.4	51.4	51.4	0.00
TiO_2	0.01	0.09	0.44	0.45	0.16	0.00	0.05	0.41	0.15	0.00	0.08	0.29	0.12	0.00	0.17	0.43	0.49	0.19	0.00	0.11	0.45	0.42	0.13
Al_2O	0.02	4.41	6.08	4.88	55.7	0.02	4.68	5.76	54.8	0.04	3.96	5.87	52.0	0.02	4.36	6.17	4.50	50.6	0.00	4.33	6.64	4.27	54.9
Cr_2O_3	0.03	0.39	0.66	0.94	10.6	0.03	0.31	0.50	8.56	0.02	0.35	0.97	13.6	0.04	0.50	0.91	1.06	14.6	0.00	0.38	0.87	0.89	10.6
FeO	9.53	6.14	3.06	3.03	11.7	13.15	8.48	4.33	16.8	10.91	7.04	3.19	13.9	9.69	6.27	3.26	3.24	12.7	9.57	6.07	3.01	2.96	11.5
MnO	0.15	0.15	0.08	0.08	0.09	0.19	0.17	0.11	0.13	0.11	0.13	0.08	0.10	0.10	0.21	0.05	0.10	0.13	0.14	0.16	0.10	0.06	0.09
MgO	49.4	32.7	15.5	16.7	20.7	46.2	31.2	15.2	18.1	48.3	32.6	15.2	19.2	49.4	33.2	15.1	16.4	20.1	49.2	32.9	15.0	17.1	20.9
CaO	0.08	0.66	20.45	22.1	0.00	0.07	0.74	21.0	0.02	0.04	0.66	20.5	0.01	0.07	0.67	19.72	22.29	0.01	0.06	0.61	20.3	22.2	0.00
Na_2O	0.01	0.11	1.64	0.40	0.00	0.00	0.02	1.03	0.01	0.00	0.08	1.23	0.00	0.02	0.13	1.86	0.44	0.00	0.00	0.07	1.65	0.32	0.00
K_2O	0.00	0.01	0.00	0.00	0.00	0.00	0.00	0.00	0.00	0.00	0.00	0.01	0.00	0.02	0.00	0.00	0.01	0.00	0.01	0.00	0.00	0.01	0.01
NiO	0.36	0.12	0.06	0.05	0.41	0.22	0.05	0.02	0.34	0.36	0.11	0.02	0.40	0.35	0.11	0.02	0.01	0.32	0.37	0.12	0.04	0.06	0.35
Total	99.0	99.6	99.8	100.5	99.3	99.1	99.5	99.8	98.9	99.1	99.4	99.2	99.2	100.4	100.8	99.4	99.7	98.8	99.5	100.1	99.6	99.6	98.5

(*continued on next page*)

Table 1 (*continued*)

Mg#	90.3	90.6	90.1	90.9	76.1	86.3	86.9	86.4	65.9	88.9	89.3	89.6	71.3	90.2	90.5	89.3	90.1	74.1	90.2	90.7	90.0	91.2	76.5
Cr#					11.4				9.49				14.9					13.6					11.5

Sample	NTS12-20					NTS12-21				MX12-01				MX12-02					MX12-03			
Rock Type	Spl lherzolite					Spl lherzolite				Spl lherzolite				Spl lherzolite					Spl lherzolite			
Mineral	Ol	Opx	Cpx	Cpx2	Spl	Ol	Opx	Cpx	Spl	Ol	Opx	Cpx	Spl	Ol	Opx	Cpx	Cpx2	Spl	Ol	Opx	Cpx	Spl
SiO_2	41.0	55.4	51.5	51.9	0.07	40.3	55.2	52.3	0.09	41.4	56.8	53.6	0.01	41.4	55.0	51.9	51.6	0.00	40.4	55.3	52.0	0.00
TiO_2	0.04	0.11	0.55	0.40	0.18	0.00	0.07	0.52	0.14	0.02	0.03	0.21	0.26	0.00	0.09	0.43	0.66	0.17	0.00	0.05	0.41	0.05
Al_2O_3	0.00	4.46	6.53	4.54	55.2	0.02	4.33	5.94	56.3	0.00	1.66	2.65	25.0	0.00	4.61	4.45	4.34	55.2	0.01	4.12	6.69	58.9
Cr_2O_3	0.03	0.29	0.86	0.84	11.6	0.00	0.32	0.66	9.20	0.02	0.51	1.26	41.6	0.05	0.44	0.93	1.11	13.5	0.00	0.32	0.81	9.51
FeO	9.85	6.42	3.26	3.16	12.4	9.83	6.47	3.03	11.6	8.29	5.51	2.11	18.5	8.92	5.62	2.79	2.95	9.79	9.81	6.21	2.27	10.4
MnO	0.15	0.15	0.07	0.09	0.11	0.14	0.16	0.07	0.08	0.07	0.13	0.07	0.15	0.11	0.15	0.07	0.08	0.10	0.14	0.10	0.09	0.04
MgO	49.2	32.8	15.2	17.2	20.3	48.5	33.4	15.6	20.7	50.7	34.9	16.5	13.7	49.7	33.0	16.3	16.4	20.5	49.5	33.5	14.7	20.4
CaO	0.07	0.78	19.9	21.9	0.00	0.06	0.67	20.7	0.03	0.01	0.46	22.3	0.00	0.08	0.72	21.7	22.0	0.01	0.04	0.50	21.3	0.02
Na_2O	0.00	0.10	1.61	0.39	0.00	0.00	0.10	1.50	0.02	0.00	0.03	1.32	0.01	0.00	0.10	0.56	0.59	0.00	0.00	0.02	1.77	0.00
K_2O	0.01	0.00	0.02	0.00	0.00	0.00	0.01	0.01	0.00	0.00	0.00	0.02	0.00	0.00	0.00	0.00	0.00	0.01	0.01	0.00	0.01	0.00
NiO	0.30	0.08	0.05	0.08	0.38	0.36	0.09	0.05	0.38	0.42	0.06	0.01	0.14	0.34	0.09	0.06	0.04	0.27	0.34	0.07	0.03	0.34
Total	100.6	100.7	99.6	100.5	100.2	99.2	100.8	100.4	98.5	100.9	100.1	100.1	99.4	100.5	99.8	99.3	99.7	99.5	100.3	100.1	100.1	99.6
Mg#	90.0	90.2	89.3	90.7	74.6	89.9	90.3	90.3	76.3	91.7	91.9	93.4	57.1	90.9	91.4	91.3	90.9	79.0	90.1	90.7	92.1	77.9
Cr#					12.3				9.88				52.8					14.1				9.78

Sample	MX12-04				MX12-05					MX12-06					MX12-07					MX12-08			
Rock type	Spl lherzolite				Spl lherzolite					Spl lherzolite					Spl lherzolite					Spl lherzolite			
Mineral	Ol	Opx	Cpx	Spl	Ol	Opx	Cpx	Cpx2	Spl	Ol	Opx	Cpx	Cpx2	Spl	Ol	Opx	Cpx	Cpx 2	Spl	Ol	Opx	Cpx	Spl
SiO_2	40.9	56.3	53.0	0.00	41.1	55.0	52.3	51.9	0.00	41.1	54.8	52.1	51.2	0.02	40.6	55.6	52.6	52.3	0.00	41.1	55.6	52.8	0.05
TiO_2	0.00	0.03	0.01	0.04	0.00	0.15	0.45	0.44	0.18	0.02	0.15	0.43	0.53	0.14	0.00	0.12	0.55	0.55	0.10	0.00	0.08	0.27	0.22
Al_2O_3	0.00	2.69	2.78	42.0	0.02	4.41	6.04	4.16	53.2	0.00	4.74	6.11	4.93	52.8	0.00	4.18	6.56	3.63	58.1	0.05	3.87	4.70	48.4
Cr_2O_3	0.01	0.50	0.76	27.8	0.06	0.51	1.01	1.06	15.7	0.00	0.44	0.86	0.97	13.9	0.02	0.29	0.71	0.66	9.11	0.03	0.58	1.00	20.6
FeO	8.50	5.46	1.81	13.2	9.18	5.80	2.63	2.28	10.7	8.91	5.72	2.53	2.78	10.4	9.69	6.19	2.32	2.87	10.5	8.64	5.46	2.46	11.1
MnO	0.15	0.17	0.06	0.13	0.17	0.14	0.12	0.04	0.06	0.17	0.12	0.08	0.12	0.07	0.17	0.13	0.04	0.04	0.04	0.09	0.12	0.11	0.10
MgO	50.3	34.3	16.9	17.1	49.9	33.2	15.8	16.8	20.5	49.5	32.9	15.7	16.0	20.7	49.4	33.0	14.7	15.6	20.6	49.8	33.2	16.6	19.6
CaO	0.03	0.40	23.5	0.02	0.05	0.75	20.2	22.9	0.00	0.08	0.78	19.9	21.7	0.00	0.01	0.52	20.7	23.2	0.01	0.06	0.81	20.9	0.01
Na_2O	0.00	0.00	0.56	0.00	0.00	0.11	1.59	0.47	0.00	0.00	0.14	1.59	0.64	0.00	0.02	0.07	1.90	0.61	0.00	0.00	0.09	1.06	0.00
K_2O	0.00	0.01	0.01	0.00	0.00	0.00	0.00	0.01	0.01	0.00	0.00	0.02	0.00	0.00	0.00	0.00	0.01	0.07	0.01	0.00	0.00	0.00	0.01
NiO	0.37	0.08	0.04	0.18	0.37	0.09	0.04	0.02	0.33	0.35	0.11	0.05	0.03	0.31	0.37	0.08	0.02	0.02	0.37	0.26	0.12	0.07	0.32
Total	100.3	100.0	99.5	100.5	100.9	100.2	100.2	100.1	100.7	100.1	99.9	99.3	99.0	98.3	100.2	100.2	100.0	99.6	98.8	100.0	100.0	100.0	100.4
Mg#	91.4	91.9	94.4	70.0	90.7	91.2	91.5	93.0	77.6	90.9	91.2	91.8	91.2	78.2	90.2	90.6	91.9	90.7	78.0	91.2	91.6	92.4	76.1
Cr#				30.7					16.6					15.0					9.51				22.2

Sample	MX12-09				MX12-10					MX12-11				MX12-12				MX12-13	
Rock type	Spl lherzolite				Spl lherzolite					Spl lherzolite				Spl lherzolite				Spl lherzolite	
Mineral	Ol	Opx	Cpx	Spl	Ol	Opx	Cpx	Cpx lamenea	Spl	Ol	Opx	Cpx	Spl	Ol	Opx	Cpx	Spl	Ol	Cpx
SiO_2	39.9	54.3	51.6	0.08	40.5	54.3	51.5	51.2	0.00	40.8	55.0	51.8	0.00	40.9	57.0	53.5	0.02	40.5	52.9
TiO_2	0.01	0.08	0.47	0.21	0.00	0.14	0.55	0.60	0.09	0.00	0.12	0.61	0.09	0.02	0.00	0.02	0.00	0.00	0.03
Al_2O_3	0.01	5.02	6.27	54.0	0.00	4.30	6.95	5.09	59.1	0.00	4.56	6.83	57.9	0.00	1.96	1.65	31.4	0.04	3.48
Cr_2O_3	0.05	0.41	0.85	12.7	0.03	0.29	0.78	0.94	8.96	0.04	0.31	0.72	9.11	0.00	0.47	0.69	38.0	0.05	1.27
FeO	9.05	5.74	3.09	11.7	9.77	6.23	2.47	2.42	10.5	9.59	6.13	2.37	10.3	8.33	5.21	1.89	13.4	8.28	2.85
MnO	0.17	0.14	0.09	0.05	0.13	0.12	0.07	0.11	0.04	0.14	0.10	0.12	0.09	0.11	0.16	0.05	0.11	0.15	0.10
MgO	49.3	32.6	15.5	20.4	49.2	33.1	14.4	16.0	20.7	49.5	32.9	14.4	20.6	50.6	34.8	17.6	16.4	50.3	18.9
CaO	0.05	0.84	19.4	0.02	0.03	0.52	20.8	22.8	0.01	0.04	0.51	20.7	0.02	0.03	0.58	23.9	0.02	0.14	20.1
Na_2O	0.01	0.12	1.71	0.02	0.02	0.05	2.01	0.64	0.00	0.00	0.04	1.84	0.00	0.00	0.01	0.20	0.01	0.00	0.31
K_2O	0.01	0.00	0.00	0.00	0.00	0.00	0.00	0.00	0.01	0.00	0.00	0.00	0.02	0.00	0.01	0.02	0.02	0.00	0.02

(*continued on next page*)

Table 1 (*continued*)

NiO	0.42	0.10	0.05	0.39	0.38	0.10	0.03	0.03		0.40	0.34	0.09	0.05	0.39	0.39	0.07	0.06	0.15	0.40	0.07
Total	99.0	99.3	99.1	99.6	100.0	99.1	99.6	99.8		99.8	100.4	99.8	99.5	98.5	100.3	100.2	99.6	99.5	99.8	100.0
Mg#	90.7	91.1	90.0	75.9	90.1	90.5	91.3	92.3		78.0	90.3	90.6	91.6	78.2	91.6	92.3	94.4	68.8	91.6	92.3
Cr#				13.7						9.23				9.56				44.8		

Sample	MX12-15			MX12-20					MXZ12-01				XL12-1				XL12-02			
Rock type	Spl dunite			Spl-grt lherzolite					Grt lherzolite				Lherzolite				Spl lherzolite			
Mineral	Ol	Cpx	Spl	Ol	Opx	Cpx	Spl	Grt[e]	Ol	Opx	Cpx	Grt	Ol	Opx	Cpx	Cpx2	Ol	Opx	Cpx	Spl
SiO_2	40.7	52.1	0.0	40.8	55.8	53.2	0.07	42.7	40.9	54.2	50.5	42.0	41.3	55.7	54.1	52.8	40.8	55.1	53.5	0.00
TiO_2	0.00	0.39	0.28	0.00	0.09	0.36	0.83	0.16	0.00	0.30	1.04	0.32	0.07	0.10	0.12	0.33	0.01	0.03	0.06	0.21
Al_2O_3	0.01	3.98	40.6	0.00	4.05	6.04	47.1	22.27	0.04	5.39	7.08	23.4	0.02	3.78	6.42	2.67	0.07	3.16	3.13	26.3
Cr_2O_3	0.05	0.85	23.1	0.02	0.34	0.85	16.3	1.96	0.02	0.66	1.10	1.46	0.01	0.57	1.26	1.57	0.07	0.99	1.14	46.1
FeO	8.94	2.08	15.5	9.88	6.34	3.05	16.8	7.02	9.79	6.16	3.52	5.81	10.27	6.46	3.17	3.09	8.63	5.40	2.93	14.9
MnO	0.16	0.08	0.08	0.14	0.12	0.09	0.06	0.26	0.15	0.11	0.11	0.24	0.11	0.09	0.04	0.03	0.12	0.04	0.04	0.18
MgO	49.4	15.6	18.6	49.3	32.6	15.3	18.5	21.0	49.8	31.5	15.9	19.4	48.5	32.4	14.8	16.3	49.0	33.2	18.9	12.9
CaO	0.06	23.6	0.02	0.05	0.65	20.4	0.02	5.16	0.10	1.11	18.9	3.92	0.06	0.72	17.5	21.8	0.14	1.65	19.88	0.01
Na_2O	0.00	0.97	0.01	0.02	0.05	1.43	0.02	0.18	0.01	0.14	1.47	3.20	0.02	0.17	2.08	0.49	0.01	0.02	0.21	0.00
K_2O	0.00	0.01	0.01	0.00	0.00	0.00	0.01	0.02	0.01	0.00	0.01	0.80	0.00	0.01	0.00	0.01	0.00	0.00	0.05	0.00
NiO	0.30	0.06	0.28	0.39	0.08	0.05	0.40	0.03	0.41	0.10	0.02	0.00	0.22	0.01	0.03	0.01	0.38	0.08	0.07	0.11
Total	99.7	99.8	98.5	100.6	100.1	100.8	100.1	100.7	101.3	99.7	99.7	100.6	100.5	100.0	99.5	99.1	99.3	99.6	99.8	100.8
Mg#	90.9	93.1	68.3	90.0	90.2	90.1	66.4	84.3	90.2	90.2	89.0	85.7	89.5	90.0	89.4	90.4	91.1	91.7	92.0	60.9
Cr#			27.6				18.8													54.1

Sample	XL12-06				XL12-7				XL12-10				XL12-11				XL12-12			
Rock type	Spl lherzolite				Spl lherzolite				Spl lherzolite				Grt lherzolite				Spl lherzolite			
Mineral	Ol	Opx	Cpx	Spl	Ol	Opx	Cpx	Sp	Ol	Opx	Cpx	Spl	Ol	Opx	Cpx	Grt	Ol	Opx	Cpx	Spl
SiO_2	41.6	55.0	53.2	0.00	41.5	54.7	52.3	0.29	41.1	53.8	52.2	0.78	41.3	53.5	52.0	40.8	41.1	54.8	52.0	0.97
TiO_2	0.10	0.14	0.14	0.43	0.05	0.01	0.68	0.08	0.03	0.12	0.73	0.17	0.00	0.14	0.73	0.12	0.00	0.01	0.68	0.18
Al_2O_3	0.04	2.98	3.13	28.2	0.01	4.59	7.04	57.6	0.00	5.00	7.28	58.3	0.10	5.54	7.07	21.08	0.04	5.51	7.53	58.1
Cr_2O_3	0.06	0.74	1.15	42.9	0.02	0.26	0.79	10.2	0.00	0.30	0.57	8.87	0.10	0.68	1.26	1.57	0.02	0.38	0.77	10.5
FeO	8.11	5.30	2.43	16.0	9.86	6.74	2.56	13.9	10.63	6.78	2.75	14.2	9.83	6.14	3.57	6.91	9.63	5.98	2.83	12.3
MnO	0.14	0.08	0.06	0.15	0.08	0.08	0.10	0.12	0.18	0.16	0.06	0.08	0.08	0.09	0.06	0.18	0.08	0.11	0.06	0.04
MgO	49.5	33.7	18.0	13.2	48.4	32.8	14.6	16.0	47.7	32.5	14.5	15.9	48.0	31.6	16.3	19.7	48.8	32.3	15.2	16.6
CaO	0.10	1.18	21.2	0.02	0.03	0.55	20.4	0.00	0.03	0.53	20.6	0.01	0.12	1.34	17.6	5.05	0.08	0.77	19.3	0.01
Na_2O	0.00	0.04	0.36	0.01	0.01	0.05	1.33	0.00	0.00	0.04	1.25	0.01	0.00	0.13	1.17	1.75	0.01	0.09	1.37	0.00
K_2O	0.00	0.01	0.01	0.00	0.00	0.00	0.01	0.01	0.00	0.00	0.00	0.00	0.00	0.01	0.01	1.03	0.00	0.00	0.00	0.00
NiO	0.31	0.06	0.01	0.10	0.25	0.04	0.04	0.29	0.26	0.00	0.03	0.21	0.24	0.07	0.05	0.05	0.26	0.08	0.00	0.27
Total	100.0	99.3	99.7	101.0	100.2	99.8	99.8	98.5	99.9	99.2	100.0	98.6	99.8	99.2	99.9	98.3	100.0	100.1	99.7	98.9
Mg#	91.7	92.0	93.0	59.7	89.8	89.8	91.1	67.4	89.0	89.6	90.5	66.8	89.8	90.3	89.2	83.7	90.1	90.7	90.6	70.8
Cr#				50.5				10.6				9.26								10.8

Sample	XL12-13				XL12-14				XL12-20				XL12-21				XL12-22			
Rock type	Spl lherzolite				Spl lherzolite				Spl lherzolite				Spl lherzolite				Spl lherzolite			
Mineral	Ol	Opx	Cpx	Spl	Ol	Opx	Cpx	Spl	Ol	Opx	Cpx	Spl	Ol	Opx	Cpx	Spl	Ol	Cpx	Cpx2	Sp
SiO_2	41.0	54.8	52.1	0.65	41.4	56.1	53.3	0.00	41.3	54.7	52.1	0.26	41.4	54.6	52.3	1.77	41.4	52.2	52.2	0.00
TiO_2	0.00	0.33	0.80	0.06	0.01	0.04	0.16	0.34	0.01	0.19	0.87	0.13	0.00	0.10	0.48	0.17	0.00	0.40	0.41	0.13
Al_2O_3	0.00	4.08	6.70	59.5	0.05	3.27	3.25	32.9	0.01	4.77	6.97	58.5	0.03	5.46	7.18	53.3	0.07	6.54	4.85	51.9
Cr_2O_3	0.00	0.18	0.43	7.08	0.02	0.66	0.87	38.3	0.00	0.33	0.58	8.34	0.02	0.50	0.93	14.2	0.02	0.85	0.89	15.3
FeO	10.7	6.80	2.59	14.0	8.08	5.11	2.25	14.6	10.74	6.99	2.78	14.1	9.54	6.11	2.97	13.2	10.20	3.10	3.25	15.0
MnO	0.12	0.10	0.10	0.11	0.13	0.07	0.05	0.15	0.10	0.11	0.10	0.10	0.11	0.11	0.04	0.06	0.04	0.07	0.09	0.13
MgO	48.1	32.5	14.5	16.0	49.8	33.9	17.6	13.7	48.4	32.5	14.7	15.9	49.0	32.2	15.7	16.1	48.2	15.6	15.8	15.5
CaO	0.03	0.49	21.3	0.01	0.10	0.94	21.5	0.01	0.04	0.48	20.8	0.01	0.09	0.89	18.96	0.01	0.09	20.0	21.7	0.01

(*continued on next page*)

Table 1 (*continued*)

Na_2O	0.00	0.04	1.11	0.02	0.00	0.02	0.29	0.00	0.00	0.04	1.29	0.00	0.01	0.09	1.24	0.00	0.00	1.26	0.76	0.00
K_2O	0.00	0.01	0.00	0.00	0.01	0.00	0.01	0.01	0.00	0.00	0.01	0.01	0.00	0.00	0.02	0.00	0.00	0.00	0.00	0.00
NiO	0.32	0.00	0.03	0.22	0.19	0.07	0.06	0.14	0.18	0.06	0.05	0.24	0.21	0.02	0.03	0.24	0.22	0.10	0.01	0.19
Total	100.4	99.2	99.7	97.6	99.9	100.2	99.3	100.2	100.8	100.2	100.3	97.6	100.4	100.1	99.8	99.2	100.3	100.1	99.9	98.2
Mg#	89.0	89.6	91.0	67.2	91.7	92.3	93.4	62.9	89.0	89.3	90.5	66.9	90.2	90.5	90.5	68.7	89.5	90.1	89.7	65.0
Cr#				7.40				43.8				8.74				15.2				16.5
Sample	XL12-23				XL12-24				XL12-25				XL12-27				XL12-28			
Rock type	Spl lherzolite				Spl lherzolite				Spl harzburgite				Spl lherzolite				Spl lherzolite			
Mineral	Ol	Opx	Cpx	Sp	Ol	Opx	Cpx	Sp	Ol	Opx	Cpx	Spl	Ol	Opx	Cpx	Spl	Ol	Opx	Cpx	Spl
SiO_2	41.4	54.5	52.3	0.00	41.5	55.0	52.2	0.00	41.6	54.9	53.3	0.00	41.5	54.4	52.2	0.13	41.3	54.4	52.9	0.00
TiO_2	0.11	0.13	0.46	0.29	0.00	0.17	0.67	0.24	0.00	0.03	0.16	0.33	0.05	0.19	0.47	0.22	0.00	0.04	0.26	0.29
Al_2O_3	0.07	5.57	7.14	53.0	0.04	5.47	7.24	53.5	0.06	3.15	3.13	26.2	0.03	4.06	6.57	55.2	0.04	4.27	5.35	41.5
Cr_2O_3	0.00	0.46	0.76	14.5	0.00	0.45	0.93	14.7	0.05	0.83	1.39	46.0	0.00	0.33	0.82	13.5	0.03	0.65	1.26	29.9
FeO	9.28	6.02	2.96	13.4	9.61	5.88	2.97	13.5	8.80	5.35	2.79	15.0	9.42	6.26	2.18	13.4	8.50	5.36	2.57	13.6
MnO	0.12	0.05	0.06	0.07	0.04	0.07	0.09	0.17	0.08	0.16	0.07	0.15	0.15	0.19	0.09	0.02	0.09	0.11	0.03	0.08
MgO	49.2	32.4	15.8	16.0	49.0	32.6	15.7	16.3	49.4	33.0	18.8	13.0	48.8	33.3	14.8	15.5	50.2	33.0	16.6	14.9
CaO	0.09	0.90	19.3	0.01	0.09	0.88	19.0	0.00	0.15	1.65	20.2	0.02	0.03	0.57	21.2	0.01	0.09	1.07	19.9	0.02
Na_2O	0.01	0.12	1.23	0.00	0.01	0.08	1.21	0.00	0.02	0.03	0.20	0.01	0.00	0.03	1.28	0.00	0.00	0.07	1.01	0.00
K_2O	0.00	0.00	0.00	0.00	0.00	0.00	0.00	0.00	0.00	0.00	0.05	0.00	0.00	0.01	0.00	0.01	0.00	0.00	0.01	0.01
NiO	0.23	0.00	0.10	0.24	0.22	0.03	0.08	0.22	0.20	0.13	0.08	0.07	0.23	0.05	0.12	0.30	0.21	0.09	0.09	0.24
Total	100.5	100.2	100.0	97.5	100.5	100.7	100.2	98.6	100.4	99.2	100.1	100.8	100.2	99.4	99.8	98.3	100.5	99.1	100.0	100.5
Mg#	90.5	90.6	90.6	68.3	90.2	90.9	90.5	68.4	91.0	91.7	92.4	60.9	90.3	90.6	92.5	67.5	91.4	91.7	92.1	66.3
Cr#				15.5				15.5				54.1				14.1				32.6

[a] Ol, olivine; Cpx, clinopyroxene; Cpx2, Spongy clinopyroxene; Opx, orthopyroxene; Spl, spinel; Grt, garnet.

Table 2
In-situ trace element data of clinopyroxene in the Niutoushan, Mingxi and Xilong peridotites (ppm) from the Cathaysia block.

Sample	NST 12–03	NST 12–10	NST 12–11	NST 12–13	NST 12–17	MX 12–01	MX 12–02	MX 12–04	MX 12–05	MX 12–06	MX 12–07	MX 12–08
Mineral	Cpx	Cpx	Cpx	Cpx	Cpx	Cpx	Cpx	Cpx	Cpx	Cpx	Cpx	Cpx
Li	8.96	2.60	11.1	3.56	6.02	10.1	15.8	12.2	26.3	17.0	8.85	20.3
Be						0.07	0.23	0.07	0.07	0.06	0.11	0.05
B						3.04	4.01	3.23	3.01	3.15	3.57	2.81
Sc	60.0	63.0	64.6	64.6	62.4	59.8	57.1	51.9	57.2	54.6	58.1	61.7
Ti	1708	2682	894	2566	1879	987	2935	199	2203	2223	3015	1353
V	221	253	223	254	235	148	260	206	242	239	256	237
Co	19.5	22.9	21.7	22.4	20.4	19.0	20.9	21.3	22.6	22.1	17.7	22.7
Ni	324	375	363	370	338	298	326	335	370	367	278	379
Cu	4.77	7.52	2.87	9.16	4.30	1.00	3.78	0.58	1.98	3.27	0.67	1.91
Zn	9.62	11.1	12.8	13.0	21.8	5.95	12.2	18.6	10.1	9.21	5.75	10.2
Ga	3.66	4.09	2.59	3.91	3.41	2.46	4.62	2.24	3.77	3.63	4.05	2.71
Ge						1.42	0.88	1.72	1.42	1.18	1.43	1.61
As						1.33	2.87	2.82	2.66	1.55	2.26	1.58
Rb	0.88	0.94	0.88	0.94	0.91	0.03	14.08	0.03	0.10	0.03	0.03	0.03
Sr	87.9	71.0	67.6	68.3	90.9	31.8	111	19.6	53.2	51.6	63.0	52.6
Y	13.0	16.8	7.58	16.4	13.7	9.03	15.5	2.79	13.7	14.0	18.8	8.31
Zr	42.5	26.6	12.4	27.0	26.8	17.0	31.7	2.99	21.6	21.3	29.3	10.9
Nb	0.59	0.60	0.59	0.69	0.58	0.06	1.47	0.37	0.10	0.14	0.03	0.13
Mo						0.12	0.11	0.09	0.07	0.06	0.06	0.07
Ag						0.15	0.23	0.17	0.16	0.18	0.16	0.15
Cd						0.10	0.19	0.19	0.11	0.17	0.18	0.41
Sn						2.02	1.70	1.71	1.84	1.59	1.84	1.27
Sb						0.04	0.11	0.09	0.09	0.09	0.10	0.07
Cs	0.41	0.43	0.43	0.49	0.42	0.01	0.41	0.02	0.01	0.01	0.01	0.01
Ba	3.03	3.26	2.70	3.31	2.95	1.19	35.43	0.09	0.15	0.04	0.08	0.09
La	7.60	1.67	3.98	1.69	8.45	0.54	4.52	1.06	0.84	0.65	0.64	0.54
Ce	14.4	3.78	7.82	3.81	19.0	1.52	11.3	2.50	2.60	2.50	2.62	1.85
Pr	1.62	0.61	0.91	0.61	2.16	0.27	1.53	0.35	0.45	0.46	0.52	0.36
Nd	6.75	3.87	3.69	3.58	9.25	2.08	7.26	1.33	2.94	3.09	3.72	2.30
Sm	1.74	1.76	1.55	1.81	2.05	0.97	1.94	0.32	1.20	1.35	1.53	0.85
Eu	0.67	0.62	0.39	0.70	0.77	0.40	0.85	0.10	0.56	0.55	0.74	0.40
Gd	2.11	2.22	1.26	2.14	2.33	1.33	2.33	0.30	1.63	2.07	2.16	1.24
Tb	0.39	0.43	0.20	0.41	0.39	0.24	0.42	0.06	0.35	0.34	0.46	0.24
Dy	2.55	3.18	1.30	3.23	2.74	1.81	2.69	0.43	2.53	2.44	3.27	1.53
Ho	0.52	0.69	0.33	0.73	0.58	0.34	0.63	0.10	0.55	0.57	0.76	0.31
Er	1.54	2.04	0.96	1.96	1.46	0.97	1.75	0.38	1.50	1.56	1.99	0.90
Tm	0.24	0.27	0.16	0.27	0.25	0.12	0.24	0.05	0.22	0.23	0.30	0.11
Yb	1.52	1.87	0.92	2.11	1.49	0.78	1.75	0.48	1.47	1.47	2.13	0.76
Lu	0.23	0.30	0.17	0.26	0.22	0.10	0.23	0.05	0.21	0.21	0.28	0.11
Hf	0.99	0.88	0.51	1.07	0.73	0.67	0.90	0.04	0.72	0.69	0.89	0.40
Ta	0.13	0.14	0.13	0.15	0.14	0.00	0.14	0.03	0.02	0.01	0.01	0.01
W						0.07	0.05	0.03	0.02	0.01	0.02	0.01
Pb	0.66	3.10	0.36	0.40	0.43	0.08	0.27	0.09	0.10	0.12	0.03	0.12
Bi						0.01	0.02	0.02	0.02	0.02	0.01	0.02
Th	1.70	0.21	0.32	0.21	1.50	0.03	0.18	0.05	0.02	0.01	0.00	0.01
U	0.40	0.17	0.16	0.17	0.25	0.01	0.06	0.02	0.00	0.01	0.05	0.00
$(La/Yb)_N$	3.59	0.64	3.10	0.57	4.06	0.50	1.85	1.59	0.41	0.32	0.21	0.51

Sample	MX 12–09	MX 12–10	MX 12–11	MX 12–13	MX 12–14	MX 12–16	MX 12–17	MX 12–18	MX 12–19	MX 12–20	XL 12–02	XL 12–06
Mineral	Cpx	Cpx	Cpx	Cpx	Cpx	Cpx	Cpx	Cpx	Cpx	Cpx	Cpx	Cpx
Li	26.0	16.8	14.9	28.66	9.90	8.89	15.3	15.6	23.1	22.1	23.3	16.1
Be	0.12	0.13	0.11	0.10	0.07	0.08	0.11	0.11	0.08	0.08	0.06	0.53
B	3.62	3.46	3.27	3.43	3.70	3.49	3.63	3.93	3.38	3.88	2.40	2.47
Sc	50.4	55.2	61.3	33.5	54.3	56.5	54.7	58.1	54.9	66.4	33.8	51.8
Ti	2329	2912	2919	132	3005	2190	3045	2612	2188	2946	436	652
V	234	252	258	166	246	241	250	258	241	271	168	188
Co	22.7	17.8	17.0	30.8	21.6	21.9	22.3	17.4	22.3	18.4	30.0	27.3
Ni	373	271	276	523	354	366	355	280	370	315	510	454
Cu	2.46	0.74	0.93	4.93	2.80	2.62	2.11	0.99	2.74	0.72	3.16	6.70
Zn	11.1	5.28	5.31	15.4	8.98	9.88	9.10	5.96	10.7	9.6	14.2	12.7
Ga	4.27	4.12	3.66	2.10	3.98	3.91	4.22	3.82	3.64	3.63	2.09	2.45
Ge	1.49	1.53	1.70	1.75	1.10	1.60	1.67	1.22	1.16	1.31	1.61	1.60
As	1.43	1.68	2.36	2.36	1.46	3.76	3.99	1.52	2.03	2.36	1.96	2.36
Rb	0.04	0.03	0.05	0.05	0.03	0.03	0.03	0.03	0.03	0.03	1.00	2.23
Sr	131	62.1	61.1	6.6	61.8	60.0	61.9	47.7	52.9	52.8	53.1	517
Y	13.9	17.1	17.5	1.40	16.9	14.2	16.6	16.9	14.1	15.8	1.62	8.68
Zr	22.5	27.1	27.6	0.34	29.3	23.1	29.2	17.0	21.7	21.8	5.5	9.5
Nb	2.34	0.04	0.03	0.35	0.08	0.25	0.11	1.32	0.13	0.15	0.64	2.28
Mo	0.06	0.05	0.06	0.09	0.04	0.07	0.08	0.07	0.08	0.08	0.02	0.04
Ag	0.16	0.16	0.22	0.18	0.16	0.17	0.18	0.16	0.24	0.15	0.13	0.13

(continued on next page)

Table 2 (*continued*)

Cd	0.17	0.11	0.19	0.10	0.14	0.15	0.14	0.17	0.12	0.09	0.11	0.10
Sn	1.71	1.84	1.67	1.36	1.64	1.66	1.97	1.88	1.53	1.65	1.20	1.84
Sb	0.08	0.07	0.08	0.08	0.07	0.09	0.09	0.09	0.08	0.06	0.09	0.22
Cs	0.01	0.02	0.01	0.01	0.01	0.01	0.01	0.01	0.02	0.01	0.02	0.11
Ba	0.10	0.03	0.08	1.22	0.08	0.09	0.08	0.06	0.12	0.84	12.5	78.2
La	4.59	0.62	0.54	0.32	0.85	1.03	0.77	1.44	0.70	0.74	1.83	7.08
Ce	10.7	2.60	2.45	0.71	3.01	3.08	3.05	3.29	2.54	2.77	5.09	12.7
Pr	1.21	0.52	0.54	0.08	0.62	0.53	0.63	0.50	0.53	0.54	0.80	1.21
Nd	5.12	3.32	3.23	0.44	3.94	3.47	3.98	2.84	2.99	3.11	3.75	4.94
Sm	1.41	1.44	1.62	0.09	1.85	1.28	1.66	1.40	1.17	1.54	0.72	1.42
Eu	0.59	0.63	0.66	0.02	0.73	0.54	0.67	0.57	0.54	0.59	0.25	0.53
Gd	1.95	2.08	2.47	0.12	2.28	1.72	2.12	1.94	1.88	1.96	0.67	1.76
Tb	0.37	0.42	0.44	0.02	0.45	0.39	0.45	0.44	0.33	0.41	0.06	0.26
Dy	2.45	3.02	3.17	0.16	3.00	2.61	2.92	2.95	2.49	2.80	0.30	1.75
Ho	0.56	0.67	0.67	0.05	0.68	0.56	0.61	0.69	0.56	0.61	0.06	0.36
Er	1.46	1.90	1.98	0.16	1.79	1.54	1.78	1.79	1.58	1.78	0.14	0.84
Tm	0.21	0.30	0.18	0.03	0.25	0.21	0.26	0.29	0.19	0.26	0.02	0.10
Yb	1.47	1.79	1.96	0.29	1.81	1.52	1.79	1.71	1.42	1.79	0.20	0.80
Lu	0.21	0.29	0.27	0.04	0.23	0.19	0.24	0.27	0.22	0.21	0.03	0.09
Hf	0.75	0.80	0.87	0.02	0.98	0.70	0.90	0.63	0.71	0.81	0.13	0.32
Ta	0.11	0.01	0.01	0.01	0.01	0.02	0.01	0.09	0.01	0.01	0.06	0.10
W	0.03	0.01	0.01	0.02	0.02	0.02	0.01	0.02	0.01	0.03	0.07	0.02
Pb	0.16	0.06	0.03	0.02	0.09	0.13	0.12	0.03	0.08	0.10	0.07	0.07
Bi	0.01	0.01	0.02	0.02	0.01	0.02	0.02	0.01	0.02	0.01	0.02	0.02
Th	0.30	0.01	0.00	0.08	0.01	0.03	0.01	0.11	0.01	0.02	0.11	0.62
U	0.06	0.01	0.00	0.01	0.01	0.01	0.01	0.04	0.00	0.01	0.01	0.14
$(La/Yb)_N$	2.23	0.25	0.20	0.80	0.34	0.48	0.31	0.61	0.35	0.30	6.65	6.34

Sample	XL 12–07	XL 12–10	XL 12–11	XL 12–12	XL 12–13	XL 12–14	XL 12–20	XL 12–21	XL 12–22	XL 12–23	XL 12–24	XL 12–27	XL 12–28
Mineral	Cpx	Cpx	Cpx	Cpx	Cpx	Cpx	Cpx	Cpx	Cpx	Cpx	Cpx	Cpx	Cpx
Li	4.94	3.62	45.6	1.56	9.45	28.8	9.07	3.22	59.1	18.5	14.9	16.0	3.69
Be	0.10	0.05	0.04	0.07		0.05	0.03	0.27	0.35	0.07	0.04	0.07	0.07
B	2.32	1.84	2.61	2.37		2.62	2.12	2.39	3.27	2.25	1.87	2.42	2.65
Sc	70.0	57.8	28.2	56.7	65.5	44.0	61.1	37.7	46.2	29.7	38.8	64.4	54.8
Ti	3149	3278	2293	2423	4740	454	3116	2208	1291	1708	2240	2257	1177
V	281	271	253	239	302	165	273	259	263	209	266	260	223
Co	18.4	20.6	27.6	22.0	18.4	27.0	19.0	23.6	23.0	35.1	24.2	18.5	24.1
Ni	291	288	420	356	271	441	279	379	346	505	394	271	407
Cu	0.71	0.66	1.34	1.53	1.67	1.89	0.54	3.17	0.85	8.49	2.30	0.60	1.03
Zn	5.7	6.6	16.7	9.44	6.96	17.4	5.80	12.4	11.5	20.1	12.4	6.69	5.87
Ga	3.77	4.96	7.31	3.82	5.08	1.63	4.53	5.77	5.53	5.31	5.25	3.36	2.78
Ge	1.48	1.52	1.57	1.75	1.77	1.27	1.81	1.41	1.66	1.51	1.12	1.00	1.10
As	2.11	2.72	2.45	1.73		2.07	2.13	2.14	5.19	2.00	1.72	2.18	2.65
Rb	0.04	0.04	0.06	0.04	0.13	0.05	0.04	0.04	0.15	0.05	0.05	0.05	0.05
Sr	31.7	34.9	62.0	81.5	57.5	41.9	35.8	81.7	296	55.9	83.4	30.8	124.6
Y	18.01	16.58	4.25	16.1	19.3	2.34	16.6	8.21	5.13	5.70	8.46	14.52	11.47
Zr	22.4	20.2	14.0	21.4	19.5	3.9	18.2	10.2	10.0	7.60	10.1	13.5	14.6
Nb	0.01	0.05	0.38	1.62	0.07	3.27	0.12	2.98	2.34	2.27	3.10	0.28	0.37
Mo	0.00	0.20	0.03	0.02	0.31	0.10	0.00	0.03	0.02	0.01	0.06	0.03	0.16
Ag	0.14	0.14	0.14	0.14		0.14	0.14	0.16	0.16	0.14	0.16	0.14	2.00
Cd	0.18	0.09	0.06	0.08		0.11	0.13	0.18	0.14	0.11	0.12	0.09	0.08
Sn	1.61	1.82	1.75	1.80		1.54	1.49	2.22	1.19	1.48	1.69	1.47	1.85
Sb	0.10	0.11	0.07	0.10		0.10	0.09	0.12	0.11	0.11	0.09	0.09	0.08
Cs	0.02	0.01	0.01	0.01	0.11	0.01	0.03	0.04	0.05	0.02	0.01	0.02	0.01
Ba	0.03	0.00	0.10	0.07	1.96	0.41	0.13	0.05	19.8	1.45	0.06	0.01	0.19
La	0.26	0.59	1.17	2.88	4.38	6.47	1.73	4.44	10.2	2.98	4.55	0.83	1.33
Ce	1.96	3.01	3.86	5.96	8.50	8.43	5.25	8.14	30.3	5.53	8.17	2.08	3.63
Pr	0.51	0.65	0.66	0.72	1.23	0.54	0.81	1.00	4.00	0.64	1.01	0.34	0.37
Nd	3.74	4.03	3.86	3.63	7.02	1.83	4.70	4.70	16.7	3.06	4.39	2.13	3.22
Sm	1.40	1.64	1.14	1.50	2.45	0.36	1.73	1.28	2.52	1.00	1.37	1.17	1.20
Eu	0.56	0.73	0.52	0.59	0.93	0.11	0.83	0.55	0.75	0.38	0.50	0.47	0.72
Gd	2.11	2.37	1.51	2.00	3.02	0.47	2.53	1.56	1.44	1.14	1.67	1.98	1.79
Tb	0.46	0.43	0.21	0.42	0.54	0.07	0.45	0.31	0.26	0.21	0.30	0.35	0.32
Dy	2.97	2.87	1.19	2.83	3.72	0.47	2.96	1.75	1.04	1.24	1.80	2.60	2.07
Ho	0.70	0.61	0.18	0.63	0.75	0.09	0.64	0.31	0.20	0.23	0.31	0.58	0.45
Er	2.05	1.80	0.41	1.67	2.08	0.29	1.71	0.71	0.51	0.55	0.75	1.66	1.16
Tm	0.27	0.26	0.05	0.25	0.30	0.05	0.27	0.07	0.07	0.05	0.07	0.23	0.13
Yb	1.91	1.94	0.21	1.64	2.02	0.33	2.06	0.56	0.51	0.36	0.49	1.69	0.97
Lu	0.26	0.24	0.03	0.27	0.28	0.04	0.21	0.04	0.07	0.04	0.06	0.23	0.11
Hf	0.88	0.73	0.55	0.70	1.41	0.27	0.66	0.50	0.39	0.37	0.60	0.65	0.59
Ta	0.00	0.01	0.04	0.04	0.02	0.17	0.01	0.16	0.30	0.14	0.17	0.01	0.02
W	0.00	0.00	0.00	0.01	0.09	0.52	0.01	0.00	0.00	0.09	0.00	0.00	0.02
Pb	0.03	0.05	0.03	0.17	0.15	0.03	0.19	0.11	0.53	0.09	0.08	0.03	0.05
Bi	0.02	0.02	0.01	0.02		0.01	0.02	0.02	0.02	0.02	0.02	0.02	0.02
Th	0.00	0.05	0.05	0.35	0.22	0.86	0.03	0.69	0.66	0.43	0.73	0.07	0.04

(*continued on next page*)

Table 2 (*continued*)

U	0.01	0.01	0.01	0.12	0.04	0.23	0.02	0.20	0.15	0.12	0.18	0.02	0.02
$(La/Yb)_N$	0.10	0.22	4.10	1.26	1.56	13.9	0.60	5.68	14.4	5.93	6.70	0.40	2.76

and Zhejiang Province lie in the west of the Zhenghe-Dapu fault, carrying abundant garnet, spinel-garnet and spinel peridotites (Xu et al., 2000, 2003; Ho et al., 2003; Yu et al., 2011; Lu et al., 2015; Liu et al., 2017). The Jiande basalts (~30 Ma) in the northwest Zhejiang Province are also located on the west of the Zhenghe-Dapu fault and entrain only spinel peridotites (Hao et al., 2014; Xiao et al., 2017).

3. Methods

All analyses in this study were performed at the Institute of Geology and Geophysics, Chinese Academy of Sciences (IGGCAS).

3.1. Elemental analyses

The major element compositions of the minerals were acquired by a JEOL JXA8100 Electron Probe, using a 15 keV accelerating voltage, a 10 nA beam current and a 5 µm beam spot. Typical analytical uncertainty for the elements analyzed was better than 1.5%. Trace elements concentrations of clinopyroxene were analyzed using a laser ablation inductively coupled plasma mass spectrometer. About 6–8 spots were measured for different clinopyroxene grains in each sample. A spot with the size of 60 µm and a repetition rate of 8 Hz were used on all minerals. The NIST 610 glass standard was used as an external calibration standard. Typical analytical precisions were generally below 5%.

3.2. In-situ Li concentration and isotopic analyses of minerals

The Li concentration and isotopic composition of olivine were carried out using Cameca IMS-1280HR SIMS, following established methods (Su et al., 2012, 2015). About 3–6 points were measured from core to rim on each grain. The O-primary ion beam was accelerated at 13 kV and an intensity of about 15–30 nA with a spot size of 20 × 30 µm. There was a substantial effect of composition on the $^7Li/^6Li$ ratio of minerals measured by secondary ion mass spectroscopy (Su et al., 2015). Li concentrations of clinopyroxene and orthopyroxene in the Niutoushan, Mingxi and Xilong peridotites are mostly higher than those of the standards by 1–2 orders of magnitude analyzed by SIMS. Such large concentration differences indicate possible matrix effect on Li concentrations and isotopic compositions of pyroxenes during analysis with SIMS, thus making the obtained values unreliable. Therefore, we only measured Li concentration and isotopic composition of olivine in this study. The Li concentration of Cpx is provided by trace element analysis. The olivine sample 06JY31Ol with Fo of 90.3 is homogeneous and was accordingly used as in-house standard (Su et al., 2015). The olivine standard in this study yielded an average δ^7Li values of 4.51 ± 0.45‰ (n = 30; 1se), consistent with the recommended values (Su et al., 2015). The analytical uncertainty (1se) was better than 1‰. Matrix effect, of which δ^7Li increased by 1.0‰ for each mole percent decrease in Mg# (> 89), was considered for calibration (Su et al., 2015).

4. Results

Mineral major element compositions of the Niutoushan, Mingxi and Xilong peridotites are listed in Table 1, whereas the trace element compositions of clinopyroxene from the xenoliths are presented in Table 2. In-situ major element composition and results of Li analyses of olivine are reported in Table 3.

4.1. Petrography and major element composition of minerals

The Niutoushan lherzolites with protogranular and granuloblastic texture are relatively fertile and have restricted Fo content of 86.3–90.9 and low Cr# of spinel of 7.22–16.7, all of which are similar to those in the Jiande Group 1 peridotites (Fo: 89.1–90.8; Cr# in spinel: 8.03–15.6) from the Cathaysia block (Table 1; Hao et al., 2014; Xiao et al., 2017). The Mingxi and Xilong spinel lherzolites have granuloblastic texture with low clinopyroxene modal composition from 6 to 15%. Relative to Niutoushan and Jiande Group 1 peridotites, minerals in the Mingxi and Xilong peridotites are characterized by more refractory components (Table 1), that is, higher Fo content in olivine (89.0–91.7); higher Cr# in spinel (7.40–54.1); and lower Al_2O_3 contents in orthopyroxene (1.66–5.62 wt%) and clinopyroxene (1.65–7.53 wt%). These features are consistent with those in the Jiande Group 2 peridotites, which have Fo content of 90.7–91.1, Cr# of spinel of 18.6–49.3, Al_2O_3 contents of 2.32–4.17 wt% in orthopyroxene and 3.65–5.69 wt% in clinopyroxene. Spongy texture in clinopyroxene is found in these three mantle xenolith suites. The boundary between spongy-textured clinopyroxenes and surrounding minerals are sharp. The spongy clinopyroxenes have higher CaO (21.7–23.2 wt%) and lower Na_2O (0.32–0.76 wt%) and Al_2O_3 (2.67–5.09 wt%) contents, compared with the primary ones (CaO: 17.5–20.7 wt%; Na_2O: 1.26–2.08 wt%; Al_2O_3: 6.04–6.95 wt%; Table 1).

4.2. Lithium concentration and isotopic composition of minerals

The Li concentrations and δ^7Li values of the olivine grains and clinopyroxene Li abundances in the Niutoushan, Mingxi and Xilong peridotites display larger variations than those in the Jiande peridotites (Tables 2 and 3; Fig. 1b–d). The Li concentration of olivine ranges from 2.59 to 4.91 ppm in the Niutoushan peridotites, from 0.56 to 9.76 ppm in the Mingxi peridotites and from 1.85 to 7.90 ppm in the Xilong peridotites (Table 3). The clinopyroxene has higher Li concentrations (2.60–11.1 ppm in the Niutoushan, 2.78–28.7 ppm in the Mingxi and 1.56–59.1 ppm in the Xilong) than that of olivine (Table 2). The δ^7Li value of olivine varies between −12.30 and +10.49‰ in the Niutoushan, between −41.08 and +1.17‰ in the Mingxi and between −52.75 and +1.82‰ in the Xilong peridotites (Table 3). Spatially, the Li concentration of olivine and clinopyroxene increases but the δ^7Li value of olivine grains decreases in the order; Niutoushan < Mingxi < Xilong peridotites (Fig. 1b–d). The basalts from the Cathayia Block also display similar trend of increasing Li and Ba contents with increasing distance from the present subduction trench (Fig. 1e and f; Huang et al., 2017; Su et al., 2017). However, the olivine and clinopyroxene of the Jiande peridotites have the mantle-like Li concentrations and isotopic compositions (Fig. 1b–d; Xiao et al., 2017). On the whole, olivines in the Niutoushan, Mingxi and Xilong peridotites display more Li enrichment but are lighter in δ^7Li value relative to those in the Jiande peridotites and other peridotites worldwide (Fig. 2).

4.3. Trace elements in clinopyroxene

Clinopyroxene in the Niutoushan, Mingxi and Xilong peridotites displays a larger variation in Primitive mantle-normalized REE patterns, ranging from spoon-shaped, convex-upward to highly LREE-enriched patterns, relative to that of Jiande Group 1 peridotites (Fig. 3a, c and e). The $(La/Yb)_N$ ratios in clinopyroxene vary from 0.57 to 4.06 in the Niutoushan peridotites, from 0.21 to 2.23 in the Mingxi peridotites, from 0.10 to 14.4 in the Xilong peridotites and from 0.06 to 0.78 in the Jiande peridotites, respectively (Table 2; Xiao et al., 2017). All the

Table 3
The Li concentration (ppm) and isotopic (‰) and major elemental composition (%) of olivine in the Niutoushan, Mingxi and Xilong peridotites from the Cathaysia block.

Sample	Mineral	Position	δ^7Li	1se	Li	1se	SiO_2	TiO_2	Al_2O_3	Cr_2O_3	FeO	MnO	MgO	CaO	Na_2O	K_2O	NiO	Total	Fo
NST12-03	Ol1	rim	2.34	0.48	3.61	0.04	40.2	0.00	0.04	0.00	9.56	0.12	48.4	0.10	0.00	0.00	0.36	98.8	90.1
		rim	1.76	0.45	3.73	0.05	40.2	0.01	0.05	0.02	9.48	0.15	48.4	0.05	0.01	0.01	0.40	98.8	90.2
		mantle	1.58	0.48	3.42	0.04	40.2	0.00	0.04	0.00	9.45	0.13	48.5	0.07	0.00	0.00	0.36	98.8	90.2
		mantle	3.57	0.43	3.56	0.04	40.3	0.01	0.06	0.05	9.54	0.15	48.6	0.07	0.00	0.00	0.39	99.1	90.2
		core	−2.87	0.45	3.71	0.04	40.8	0.01	0.04	0.02	9.57	0.16	48.6	0.05	0.01	0.00	0.36	99.7	90.1
		core	−7.36	0.40	4.56	0.04	41.2	0.01	0.04	0.00	9.67	0.14	48.6	0.07	0.01	0.00	0.39	100	90.0
	Ol2	rim	−6.57	0.46	4.03	0.05	40.7	0.00	0.05	0.01	9.51	0.14	49.0	0.06	0.00	0.01	0.33	100	90.3
		rim	−3.85	0.47	3.91	0.05	40.9	0.06	0.03	0.01	9.53	0.15	49.0	0.07	0.00	0.00	0.39	100	90.3
		core	3.12	0.52	3.48	0.04	40.8	0.00	0.04	0.00	9.49	0.14	48.6	0.05	0.02	0.01	0.33	99.4	90.2
		core	3.32	0.49	3.41	0.04	40.7	0.02	0.01	0.00	9.52	0.16	48.4	0.05	0.00	0.00	0.39	99.3	90.1
NTS12-10	Ol1	rim	4.24	0.29	3.85	0.05	39.9	0.00	0.03	0.05	9.45	0.14	48.9	0.08	0.00	0.00	0.40	98.9	90.3
		mantle	4.22	0.33	2.85	0.03	40.1	0.00	0.04	0.04	9.37	0.13	48.9	0.06	0.00	0.00	0.41	99.0	90.4
		core	10.49	0.31	2.80	0.04	40.3	0.01	0.04	0.03	9.36	0.12	48.9	0.06	0.00	0.00	0.39	99.2	90.4
	Ol2	rim	4.99	0.35	2.59	0.03	40.4	0.02	0.04	0.00	9.37	0.16	48.3	0.09	0.01	0.00	0.39	98.7	90.3
		mantle	4.90	0.32	2.75	0.04	40.5	0.00	0.05	0.00	9.41	0.15	48.3	0.10	0.00	0.00	0.39	98.9	90.2
		core	5.70	0.38	2.81	0.03	40.9	0.00	0.05	0.00	9.38	0.12	48.2	0.10	0.00	0.01	0.44	99.3	90.3
	Cpx1	rim	−0.32	0.37	2.42	0.02	52.6	0.41	6.52	0.68	3.10	0.09	15.1	19.9	1.72	0.00	0.07	100	89.7
		mantle	3.48	0.96	2.52	0.06	51.7	0.49	4.82	0.86	3.35	0.12	16.6	21.4	0.61	0.00	0.10	100	89.9
		core	0.71	0.35	2.70	0.02	52.3	0.43	6.22	0.74	3.11	0.08	15.3	19.8	1.68	0.00	0.02	99.5	89.8
NST12-11	Ol1	rimrimim	−4.46	0.54	3.06	0.04	41.0	0.00	0.06	0.02	9.64	0.13	48.4	0.05	0.01	0.00	0.37	99.7	90.0
		core	−3.43	0.61	2.81	0.03	41.2	0.02	0.03	0.00	9.66	0.12	48.6	0.08	0.00	0.00	0.38	100	90.1
	Ol2	rim	−12.30	0.44	2.99	0.04	41.1	0.01	0.03	0.00	9.57	0.13	48.8	0.07	0.00	0.01	0.36	100	90.2
		mantle	−2.08	0.56	2.62	0.03	40.5	0.01	0.04	0.03	9.63	0.15	48.8	0.07	0.00	0.00	0.39	99.5	90.1
		mantle	−1.30	0.48	2.81	0.03	40.6	0.01	0.05	0.01	9.64	0.13	48.6	0.08	0.00	0.00	0.40	99.5	90.1
		core	−4.31	0.53	2.69	0.03	40.2	0.00	0.05	0.02	9.69	0.12	48.9	0.07	0.00	0.01	0.39	99.4	90.1
		core	−8.33	0.50	2.73	0.03	40.1	0.01	0.04	0.02	9.63	0.16	48.0	0.09	0.01	0.00	0.38	98.4	90.0
NST12-13	Ol1	rim	7.35	0.47	2.80	0.03	39.8	0.02	0.07	0.00	9.92	0.15	48.2	0.08	0.02	0.01	0.36	98.7	89.7
		mantle	8.01	0.49	2.79	0.03	39.7	0.00	0.06	0.00	9.94	0.15	48.5	0.08	0.00	0.00	0.42	98.9	89.8
		core	6.92	0.47	2.98	0.04	39.7	0.00	0.06	0.01	9.97	0.12	48.6	0.11	0.00	0.00	0.37	99.0	89.8
	Ol2	rim	7.03	0.56	2.99	0.04	40.1	0.01	0.05	0.00	10.3	0.19	48.6	0.12	0.02	0.00	0.38	99.6	89.5
		mantle	7.54	0.51	2.90	0.04	39.8	0.00	0.06	0.00	10.2	0.13	48.7	0.07	0.00	0.00	0.39	99.3	89.6
		core	7.40	0.50	3.26	0.04	39.9	0.00	0.05	0.00	10.3	0.11	48.5	0.08	0.00	0.00	0.36	99.2	89.5
		core	6.78	0.46	3.25	0.04	40.2	0.00	0.03	0.00	10.3	0.14	48.5	0.06	0.00	0.00	0.40	99.7	89.4
		mantle	8.54	0.41	2.95	0.04	40.4	0.02	0.07	0.00	10.3	0.14	48.3	0.08	0.00	0.01	0.38	99.7	89.4
		rim	8.12	0.43	2.86	0.03	40.6	0.00	0.03	0.01	10.1	0.14	48.2	0.08	0.01	0.01	0.45	99.7	89.6
NST12-17	Ol1	rim	3.93	0.32	4.31	0.05	40.8	0.01	0.06	0.00	12.1	0.14	46.8	0.08	0.00	0.00	0.38	100	87.5
		mantle	3.82	0.27	4.30	0.05	40.7	0.01	0.05	0.02	12.0	0.15	46.8	0.05	0.00	0.00	0.36	100	87.6
		core	4.08	0.31	4.30	0.05	40.5	0.01	0.04	0.01	12.0	0.13	46.7	0.04	0.00	0.00	0.36	99.9	87.5
	Ol2	rim	3.80	0.27	4.31	0.05	40.6	0.02	0.03	0.01	11.8	0.14	46.7	0.07	0.05	0.02	0.34	99.7	87.7
		mantle	3.24	0.28	4.31	0.05	40.7	0.00	0.05	0.03	11.8	0.11	47.0	0.05	0.00	0.00	0.36	100	87.7
		core	2.81	0.30	4.21	0.05	40.5	0.02	0.04	0.00	11.9	0.14	46.7	0.06	0.00	0.00	0.37	99.7	87.6
MX12-01	Ol1	rim	−7.04	0.34	4.26	0.05	40.9	0.01	0.02	0.02	8.50	0.11	48.0	0.01	0.00	0.01	0.40	98.0	91.0
		rim	−6.55	0.34	3.43	0.04	41.6	0.00	0.02	0.00	8.38	0.13	49.0	0.02	0.01	0.00	0.37	99.5	91.3
		mantle	−4.08	0.40	3.07	0.04	41.5	0.00	0.04	0.02	8.31	0.10	48.6	0.03	0.00	0.00	0.37	98.9	91.3
		core	−1.61	0.33	3.08	0.04	41.6	0.00	0.03	0.00	8.24	0.13	48.3	0.01	0.01	0.00	0.40	98.7	91.3
	Ol2	rim	−8.91	0.37	5.86	0.07	41.9	0.03	0.03	0.00	8.56	0.13	48.5	0.05	0.00	0.00	0.40	99.7	91.1
		mantle	−12.00	0.45	3.87	0.04	41.4	0.05	0.02	0.01	8.26	0.11	49.0	0.02	0.00	0.00	0.40	99.2	91.4
		core	−0.42	0.47	2.92	0.03	41.5	0.03	0.04	0.01	8.27	0.10	49.0	0.04	0.03	0.00	0.35	99.4	91.4
		core	−0.80	0.51	2.88	0.03	41.3	0.00	0.05	0.00	8.25	0.12	49.2	0.02	0.01	0.00	0.39	99.4	91.5
		mantle	−4.75	0.55	2.66	0.03	41.4	0.00	0.05	0.00	8.30	0.11	48.7	0.02	0.00	0.00	0.42	99.0	91.3
		rim	−5.90	0.53	2.85	0.03	42.1	0.00	0.01	0.00	8.51	0.10	48.7	0.00	0.00	0.00	0.40	99.8	91.2
MX12-04	Ol1	rim	0.94	0.35	7.94	0.10	40.2	0.00	0.03	0.00	8.57	0.14	49.8	0.07	0.00	0.00	0.38	99.1	91.3
		mantle	−6.66	0.45	7.56	0.09	40.0	0.00	0.06	0.02	8.44	0.12	49.4	0.03	0.02	0.00	0.36	98.5	91.3
		core	1.17	0.59	1.92	0.02	40.7	0.02	0.03	0.00	8.53	0.10	49.6	0.02	0.00	0.00	0.35	99.3	91.3
		core	−0.62	0.56	1.88	0.02	40.7	0.00	0.02	0.00	8.62	0.11	49.8	0.02	0.00	0.00	0.42	99.7	91.2
		mantle	−17.81	0.37	6.27	0.07	41.1	0.02	0.04	0.02	8.57	0.15	49.1	0.02	0.00	0.00	0.42	99.4	91.2
		rim	−6.43	0.38	9.76	0.10	41.0	0.01	0.05	0.02	8.34	0.15	49.2	0.05	0.00	0.01	0.39	99.2	91.4
	Ol2	rim	−6.45	0.37	7.22	0.09	40.9	0.02	0.05	0.00	8.55	0.13	49.3	0.02	0.00	0.03	0.36	99.3	91.2
		rim	−22.49	0.38	5.15	0.06	40.9	0.00	0.04	0.00	8.57	0.12	49.6	0.02	0.00	0.00	0.38	99.6	91.2
		mantle	−0.50	0.70	1.81	0.02	41.0	0.00	0.04	0.01	8.64	0.14	49.7	0.01	0.00	0.00	0.40	99.8	91.2
		core	−17.52	0.55	2.15	0.03	40.9	0.03	0.02	0.02	8.50	0.16	49.6	0.02	0.01	0.01	0.38	99.7	91.3
MX12-12	Ol1	rim	−1.69	0.30	8.12	0.10	41.3	0.00	0.03	0.03	8.45	0.11	48.9	0.01	0.01	0.00	0.41	99.3	91.2
		mantle	−15.72	0.39	6.60	0.08	41.3	0.00	0.01	0.01	8.42	0.11	49.0	0.03	0.02	0.00	0.41	99.2	91.3
		core	−22.25	0.42	4.05	0.05	41.2	0.00	0.05	0.00	8.43	0.12	47.9	0.01	0.00	0.01	0.42	98.1	91.1
		core	−23.58	0.45	3.86	0.05	41.3	0.00	0.03	0.00	8.46	0.08	47.6	0.04	0.00	0.01	0.41	98.0	91.0
		mantle	−15.78	0.34	7.20	0.08	40.8	0.01	0.04	0.00	8.49	0.11	49.6	0.03	0.01	0.01	0.41	99.5	91.3
		rim	−0.20	0.34	7.12	0.08	41.4	0.02	0.04	0.01	8.46	0.14	49.0	0.03	0.02	0.01	0.39	99.5	91.3
	Ol2	rim	−21.68	0.47	2.68	0.03	41.3	0.02	0.03	0.01	8.42	0.11	49.1	0.03	0.00	0.00	0.41	99.4	91.3
		mantle	−30.84	0.37	3.85	0.04	40.9	0.01	0.05	0.03	8.42	0.12	49.2	0.02	0.00	0.00	0.44	99.1	91.3
		core	−24.11	0.48	3.17	0.04	40.5	0.00	0.05	0.00	8.46	0.12	49.4	0.02	0.00	0.00	0.41	99.0	91.3
MX12-13	Ol1	rim	−28.50	0.24	7.27	0.10	41.3	0.01	0.08	0.08	8.51	0.13	49.2	0.15	0.00	0.00	0.41	99.9	91.2
		mantle	−12.77	0.36	2.02	0.03	41.1	0.01	0.06	0.04	8.56	0.10	49.3	0.16	0.00	0.01	0.41	99.7	91.2
		core	−4.88	0.39	1.93	0.02	41.0	0.01	0.08	0.03	8.44	0.15	49.6	0.15	0.00	0.00	0.38	99.8	91.4

(*continued on next page*)

Table 3 (*continued*)

Sample	Mineral	Position	δ^7Li	1se	Li	1se	SiO_2	TiO_2	Al_2O_3	Cr_2O_3	FeO	MnO	MgO	CaO	Na_2O	K_2O	NiO	Total	Fo
		mantle	−10.79	0.36	2.04	0.03	40.7	0.00	0.07	0.06	8.36	0.14	49.4	0.14	0.00	0.00	0.41	99.3	91.4
		rim	−28.18	0.35	2.95	0.04	40.3	0.00	0.08	0.05	8.50	0.11	49.5	0.18	0.00	0.00	0.39	99.1	91.3
	Ol2	rim	−26.97	0.26	6.74	0.07	41.6	0.00	0.07	0.06	8.54	0.14	48.7	0.16	0.00	0.00	0.36	99.6	91.1
		mantle	−33.48	0.30	4.18	0.05	41.4	0.01	0.07	0.06	8.36	0.12	48.8	0.17	0.00	0.00	0.41	99.4	91.3
		core	−29.89	0.31	2.77	0.03	41.5	0.01	0.09	0.06	8.49	0.13	48.7	0.16	0.00	0.00	0.42	99.5	91.2
MX12-15	Ol1	rim	−34.20	0.26	6.32	0.08	41.2	0.01	0.02	0.01	9.33	0.12	49.0	0.04	0.00	0.00	0.36	100	90.4
		rim	−44.40	0.26	4.59	0.06	41.0	0.00	0.02	0.00	9.23	0.14	48.7	0.06	0.00	0.00	0.32	99.5	90.5
		mantle	−40.95	0.32	3.18	0.04	41.2	0.02	0.04	0.01	9.25	0.16	49.0	0.05	0.00	0.01	0.35	100	90.5
		mantle	−10.19	0.23	7.68	0.10	40.9	0.03	0.03	0.00	9.16	0.13	48.7	0.06	0.02	0.00	0.34	99.4	90.5
		core	−2.01	0.22	6.90	0.09	41.0	0.00	0.04	0.00	9.43	0.15	48.8	0.08	0.00	0.00	0.35	99.8	90.3
	Ol2	rim	−29.00	0.37	2.37	0.03	41.0	0.00	0.03	0.01	9.27	0.15	48.8	0.04	0.00	0.02	0.34	99.6	90.5
		mantle	−0.44	0.33	1.90	0.02	40.8	0.01	0.03	0.00	9.41	0.17	49.0	0.06	0.00	0.00	0.34	99.9	90.4
		core	−9.03	0.33	2.08	0.03	40.8	0.00	0.04	0.00	9.18	0.12	48.8	0.07	0.00	0.01	0.35	99.4	90.5
	Ol3	rim	−41.08	0.34	4.04	0.05	40.9	0.03	0.04	0.02	9.18	0.13	48.9	0.07	0.01	0.00	0.35	99.6	90.6
		core	−9.26	0.42	2.01	0.02	41.8	0.00	0.03	0.00	9.68	0.15	49.0	0.09	0.00	0.01	0.33	101	90.1
MX12-20	Ol1	rim	−14.75	0.53	2.96	0.02	40.8	0.03	0.10	0.05	10.60	0.15	46.9	0.12	0.01	0.00	0.34	99.1	88.9
		mantle	−7.44	0.83	1.08	0.01	40.9	0.06	0.10	0.04	10.37	0.14	47.1	0.11	0.02	0.00	0.36	99.2	89.1
	Ol2	rim	−7.79	0.52	3.42	0.06	40.1	0.01	0.10	0.05	10.80	0.17	47.6	0.18	0.00	0.01	0.30	99.4	88.8
		mantle	−10.88	0.77	1.36	0.02	40.3	0.02	0.07	0.02	10.60	0.15	47.6	0.12	0.00	0.01	0.37	99.2	89.0
	Ol3	rim	−27.10	0.55	1.42	0.01	40.8	0.04	0.05	0.04	10.64	0.12	47.3	0.12	0.03	0.01	0.40	99.6	88.9
		mantle	−17.42	0.97	0.56	0.01	40.5	0.02	0.08	0.04	10.48	0.16	47.4	0.10	0.02	0.00	0.39	99.1	89.1
		core	−24.09	0.87	0.95	0.01	40.7	0.01	0.08	0.03	10.52	0.14	47.6	0.11	0.00	0.00	0.40	99.6	89.1
XL12-02	Ol1	rim	−1.85	0.57	2.11	0.02	40.5	0.02	0.07	0.05	9.01	0.13	48.4	0.15	0.00	0.00	0.37	98.7	90.6
		rim	0.99	0.52	1.94	0.02	40.6	0.00	0.07	0.08	8.63	0.12	48.9	0.13	0.01	0.00	0.38	98.9	91.1
		mantle	1.73	0.60	1.95	0.02	40.3	0.01	0.07	0.07	8.61	0.13	49.5	0.12	0.01	0.00	0.41	99.2	91.2
		mantle	1.54	0.63	1.95	0.02	40.8	0.00	0.08	0.11	8.49	0.08	49.1	0.13	0.03	0.00	0.40	99.3	91.2
		core	0.68	0.54	1.92	0.02	40.7	0.01	0.06	0.06	8.56	0.11	49.5	0.12	0.00	0.01	0.41	99.5	91.2
	Ol2	rim	−13.50	0.49	2.81	0.03	40.7	0.00	0.06	0.05	8.53	0.11	49.1	0.15	0.00	0.01	0.40	99.1	91.2
		rim	0.94	0.57	2.00	0.02	40.7	0.01	0.06	0.06	8.53	0.14	49.3	0.13	0.00	0.00	0.37	99.3	91.2
		mantle	1.82	0.53	1.99	0.02	41.3	0.00	0.07	0.08	8.62	0.12	49.0	0.16	0.00	0.00	0.35	99.7	91.1
		mantle	0.49	0.58	2.13	0.02	41.1	0.05	0.07	0.07	8.69	0.11	48.6	0.15	0.00	0.00	0.35	99.2	91.0
		core	0.73	0.64	1.95	0.02	41.2	0.02	0.08	0.10	8.67	0.13	49.0	0.14	0.02	0.00	0.34	99.7	91.0
XL12-06	Ol1	rim	−14.03	0.43	5.53	0.06	40.8	0.01	0.06	0.02	8.15	0.11	49.6	0.09	0.00	0.02	0.37	99.2	91.6
		mantle	−31.55	0.43	4.25	0.05	40.2	0.01	0.06	0.05	8.13	0.14	49.8	0.09	0.00	0.00	0.38	98.9	91.7
		core	−32.59	0.46	3.00	0.03	40.1	0.00	0.05	0.02	8.08	0.14	49.8	0.09	0.00	0.00	0.39	98.7	91.7
	Ol2	rim	−22.78	0.44	4.25	0.05	39.9	0.00	0.05	0.05	8.33	0.15	49.9	0.11	0.00	0.00	0.36	98.9	91.5
		rim	−25.08	0.45	4.15	0.05	39.8	0.02	0.05	0.03	8.23	0.12	50.0	0.09	0.02	0.00	0.39	98.7	91.6
		mantle	−25.85	0.47	3.81	0.04	40.0	0.02	0.05	0.06	8.12	0.13	50.0	0.10	0.04	0.01	0.36	98.9	91.7
		mantle	−20.31	0.54	2.31	0.03	39.8	0.02	0.05	0.03	8.05	0.09	49.6	0.08	0.00	0.02	0.38	98.2	91.7
		core	−14.23	0.60	2.14	0.02	40.1	0.00	0.06	0.03	8.32	0.12	50.2	0.10	0.00	0.00	0.38	99.3	91.6
XL12-28	Ol1	rim	−29.44	0.54	2.86	0.04	40.4	0.00	0.06	0.04	8.33	0.10	48.5	0.11	0.02	0.00	0.34	97.9	91.3
		mantle	−2.91	0.57	1.90	0.02	40.4	0.00	0.06	0.00	8.31	0.11	49.0	0.08	0.01	0.01	0.36	98.4	91.4
		core	0.06	0.50	1.86	0.02	41.0	0.02	0.07	0.05	8.41	0.12	49.2	0.09	0.02	0.00	0.39	99.4	91.3
		core	0.24	0.59	1.88	0.02	40.8	0.00	0.05	0.02	8.19	0.13	49.3	0.07	0.01	0.00	0.37	98.9	91.6
		mantle	−52.75	0.36	6.12	0.08	41.1	0.02	0.07	0.05	8.55	0.14	49.0	0.09	0.00	0.01	0.35	99.4	91.2
		rim	−26.58	0.38	7.90	0.09	41.1	0.02	0.06	0.03	8.36	0.12	48.2	0.08	0.02	0.00	0.37	98.4	91.2
	Ol2	rim	−35.55	0.49	2.51	0.03	41.1	0.00	0.05	0.04	8.48	0.13	48.6	0.09	0.01	0.00	0.39	98.8	91.2
		mantle	−1.94	0.48	1.90	0.02	41.1	0.00	0.07	0.05	8.18	0.12	48.7	0.07	0.01	0.00	0.35	98.7	91.5
		core	−1.30	0.51	1.85	0.02	41.2	0.00	0.05	0.03	8.29	0.15	48.7	0.07	0.03	0.00	0.39	98.9	91.4

clinopyroxenes in these four suites display negative anomalies in high field strength elements (HFSE; e.g., Zr, Nb, and Ti; Fig. 3b, d and f). The Th, U and Sr exhibit some enrichment especially in the Mingxi and Xilong peridotites where other elements do not show enrichment (Fig. 3 b, d and f).

5. Discussion

5.1. Melting history and mantle metasomatism in the lithospheric mantle beneath the Cathaysia block

Clinopyroxene in mantle peridotite is the dominant repository for most trace elements, and it can be used to reveal mantle processes, such as melt extraction and metasomatism (Zangana et al., 1999). The HREE (e.g., Y and Yb) concentrations of clinopyroxene are generally weakly affected by later metasomatic processes in the anhydrous system, and therefore can be used to estimate the degree of partial melting of peridotites (Norman 1998). Modeling of Y and Yb contents in clinopyroxene suggests that Niutoushan and Jiande Group 1 peridotites were probably produced by < 5% fractional melting from a primitive source, while most Mingxi and Xilong xenoliths, as well as Jiande Group 2, peridotites experienced 10–20% fractional melting (Fig. 4a).

In this study, the clinopyroxene trace element patterns of the Niutoushan, Mingxi and Xilong peridotites also reflect multi-stage mantle processes (Fig. 3). Clinopyroxenes with spoon-shaped trace element patterns may be affected by chromatographic metasomatism during which the enrichment front of the highly incompatible elements migrated faster than that of less compatible elements (Fig. 3a; Navon and Stolper, 1987). The convex-upward REE pattern confirms the combination of at least two events, an earlier stage of partial melting to deplete the rock in LREE and MREE, and a later stage of metasomatism that resulted in the enrichment of LREE and other LILE (Fig. 3a; O'Reilly et al., 1991). The LREE-enriched patterns also reveal significant metasomatism (Fig. 3a). Various metasomatic agents have been proposed to account for the enrichment of mantle peridotites including alkali-rich silicate melts (Wulff-Pedersen et al., 1996; Zangana et al., 1997), H_2O- ± CO_2-rich fluids (O'Reilly and Griffin, 1988; Downes, 2001) and carbonatitic melts (Rudnick et al., 1993; Yaxley et al., 1998; Coltorti et al., 1999). Coltorti et al., (1999) showed a world-wide compilation trace element data of clinopyroxenes from mantle

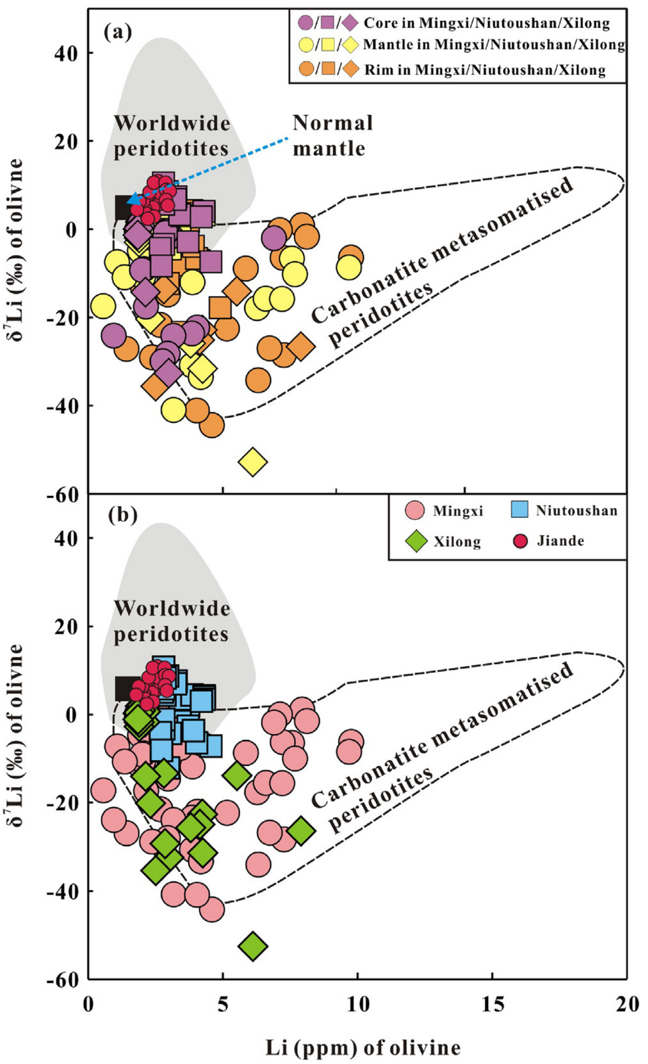

Fig. 2. Correlation of Li concentrations and δ^7Li values of olivine in the Niutoushan, Mingxi, Xilong and Jiande peridotites from the Cathaysia Block compared to worldwide olivine data (a, b). The normal mantle value and field of carbonatite metasomatized peridotites are defined by Woodland et al. (2004) and Su et al. (2014). Jiande peridotite data shown for comparison are from Xiao et al. (2017). The field of Li data from worldwide localities are from Seitz et al. (2004), Magna et al. (2006, 2008), Jeffcoate et al. (2007), Rudnick and Ionov (2007), Tang et al. (2007, 2011), Wagner and Deloule (2007), Aulbach et al. (2008), Ionov and Seitz (2008), Aulbach and Rudnick (2009), Halama et al. (2009), Zhang et al. (2010) and Xiao et al. (2015).

peridotites inferred to have been metasomatized by a spectrum of agents ranging from carbonatitic to silicic melts. The clinopyroxene trace element data from Niutoushan, Mingxi and Xilong peridotites in this study and literatures also show a broad variation covering the fields for both silicate and carbonatite metasomatism (Fig. 4c; Xu et al., 2000, 2003; Yu et al., 2011; Lu et al., 2015; Liu et al., 2017). On the other hand, petrological features of the mantle xenoliths in the Niutoushan, Mingxi and Xilong localities in the literature also suggested that the mantle beneath the Cathaysia block has undergone modal metasomatism such as the occurrence of phlogopite, amphibole and apatite (Xu et al., 2000, 2003; Liu et al., 2017). In addition, the metasomatic enrichment in LREE is accompanied in most cases by enrichment in Sr in these mantle peridotites (Figs. 3b and 4b). These indicate that the metasomatic agent may be H_2O-rich melt/fluid. Therefore, the lithospheric mantle beneath Niutoushan, Mingxi and Xilong may have been subjected to multi-stage metasomatism after partial melting, which might be pervasive in the lithospheric mantle beneath the Cathaysia block (Xu et al., 2000, 2003; Yu et al., 2011; Lu et al., 2015; Liu et al., 2017).

5.2. Spatial and temporal heterogeneity of Li isotopes beneath the Cathaysia block

In the upper mantle, fertile to moderately depleted peridotites are estimated to have Li concentration of 1.0–2.2 ppm in olivine and 0.5–1.3 ppm for pyroxene (Seitz and Woodland, 2000), and Li partitioning among equilibrated peridotite minerals follows the order Ol > Cpx ≥ Opx > Spl (Grt) (Seitz and Woodland, 2000; Halama et al., 2009). In this study, most olivine grains have lower Li concentration than coexisting clinopyroxene grains, indicating a disequilibrium between the olivine and pyroxene. Due to the moderate incompatibility of Li, melt depletion leads to lower concentrations in all minerals such as most Jiande lherzolites (Fig. 2; Xiao et al., 2017). However, anomalously higher Li concentrations (up to 9.76 ppm in olivine and 59.1 ppm in clinopyroxene) of minerals are evident in the peridotites from the Niutoushan, Mingxi and Xilong localities, compared to the published Li elemental data of olivine worldwide and normal mantle, suggesting significant Li addition from the infiltrating melt. (Figs. 1b, d and 2; Seitz and Woodland, 2000; Woodland et al., 2004; Tomascak et al., 2016).

Diffusion-driven fractionation of Li isotopes is the most important mechanism for inter-mineral Li isotopic disequilibrium, which may result from closed-system Li-redistribution, Li diffusion from melt/host magma into entrained xenoliths or metasomatism (Jeffcoate et al., 2007; Rudnick and Ionov, 2007; Tang et al., 2007; Wagner and Deloule, 2007; Aulbach et al., 2008; Aulbach and Rudnick, 2009; Su et al., 2012, 2014, 2018; Weyer and Seitz, 2012; Lai et al., 2015). The diffusion coefficients of Li in olivine range from $1 \times 10^{-11}\,m^2\,s^{-1}$ in olivine (Dohmen et al., 2010), while Coogan et al. (2005) determined the diffusion coefficient of Li in clinopyroxene which is found to range between 5×10^{-15} and $4 \times 10^{-12}\,m^2\,s^{-1}$ at temperatures of 800–1100 °C. The Li diffusion in olivine is much slower than the rates of Li diffusion in clinopyroxene (Coogan et al., 2005; Dohmen et al., 2010; Jeffcoate et al., 2007; Parkinson et al., 2007; Rudnick and Ionov, 2007). Thus, the light Li isotope signatures in mineral phases can be explained by inter-mineral Li-redistribution during cooling (Jeffcoate et al., 2007; Ionov and Seitz, 2008; Gao et al., 2011). However, closed-system Li-redistribution would only cause low Li concentration and high δ^7Li value in olivine, in combination with high Li concentration in coexisting clinopyroxene, which is different from that in our studies. On the other hand, the faster diffusion rate in clinopyroxene can also induce the observed isotopically heavy cores with lower Li concentrations than the light rims in minerals especially clinopyroxene from host magma (Jeffcoate et al., 2007; Rudnick and Ionov, 2007; Wagner and Deloule, 2007; Aulbach et al., 2008; Aulbach and Rudnick, 2009; Lai et al., 2015; Gu et al., 2016). However, the Li concentration in the host magma ranges from 3.90 to 6.20 ppm in the Niutoushan basalts, from 9.10 to 12.7 ppm in the Mingxi basalts and from 14.7 to 18.0 ppm in the Xilong basalts (Huang et al., 2017), all of which are much lower than those in clinopyroxene from these peridotites (Fig. 1b and e). Moreover, most olivine grains in the Niutoushan, Mingxi and Xilong peridotites display lower δ^7Li values but high Li concentrations in the rims than in the cores (Table 3). Their cores also display negative δ^7Li values, even when their Li concentration plateaus (Fig. 2a). Thus, the model of diffusive ingress of Li from the host magma can be rule out. In this study, the δ^7Li value and Li concentration of olivine from Niutoushan, Xilong and Mingxi peridotites shows large variations, while that from Jiande peridotites is homogenous (Fig. 5a and b). The Li/Yb ratio of the clinopyroxene shows an extreme range between 0.95 and 222 in the Niutoushan, Mingxi and Xilong peridotites, and is slightly higher than Li/Yb variability in metasomatized mantle xenoliths (< 40; Ionov and Seitz, 2008; Pogge von Strandmann et al., 2011) and Jiande peridotites (0.29–3.02; Xiao et al., 2017). Therefore, the variable Li concentration

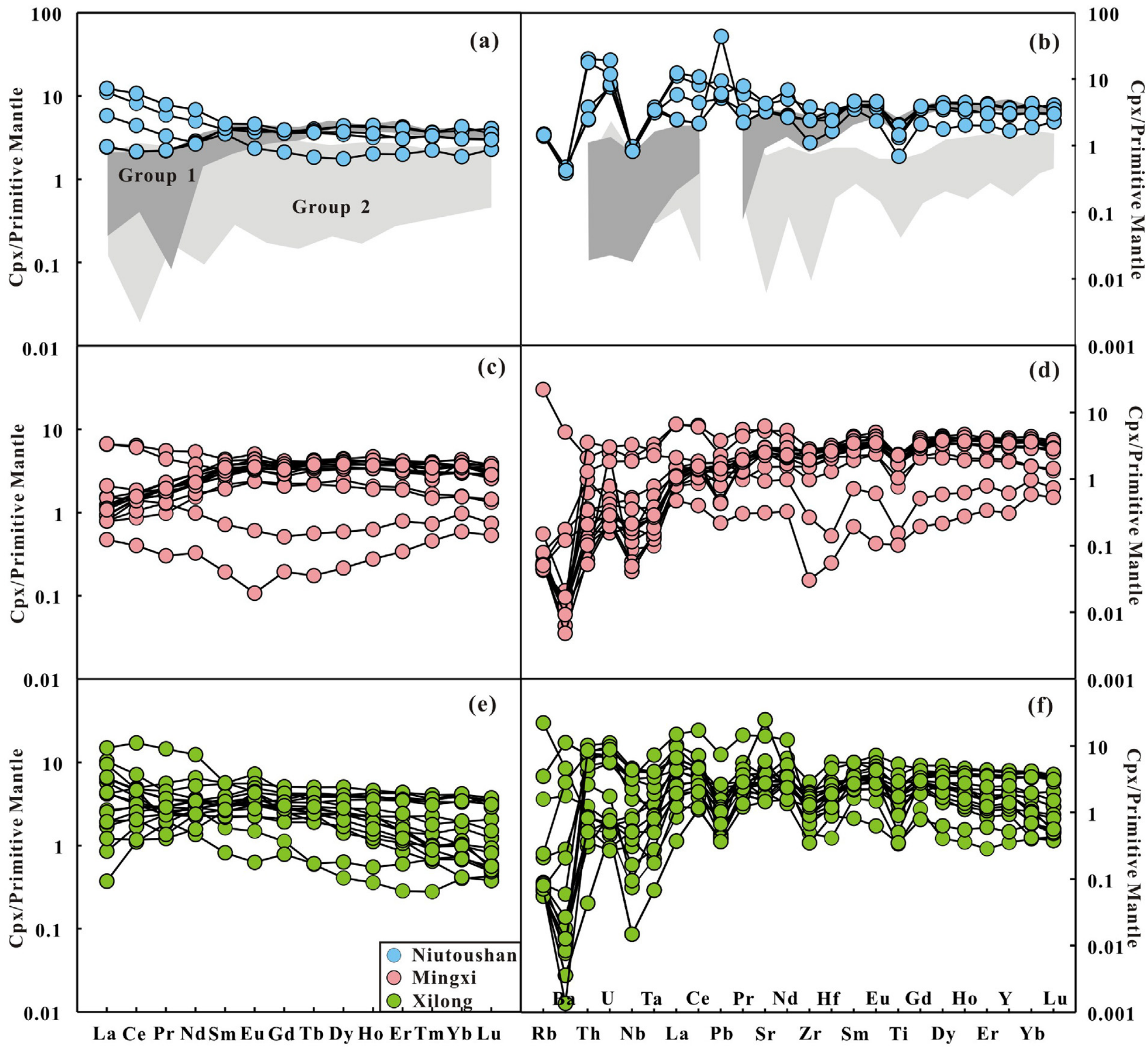

Fig. 3. Primitive mantle-normalized rare earth element pattern (a, c, e) and trace element pattern (b, d, e) of clinopyroxene in peridotites from the Niutoushan, Mingxi and Xilong localities. The rare earth element and trace element were normalized to the primitive mantle (McDonough and Sun,1995). The dark and light grey areas represent clinopyroxene from the Jiande Group 1 and 2 peridotites, respectively (Xiao et al., 2017).

and δ^7Li value of olivine and clinopyroxene Li concentration in the Niutoushan, Mingxi and Xilong peridotites may record mantle metasomatism prior to entrainment by the host magma.

The higher diffusivity of Li in clinopyroxene compared with olivine would result in higher Li concentrations in metasomatized clinopyroxene (Jeffcoate et al., 2007; Rudnick and Ionov, 2007). In this study, the clinopyroxene grains have higher Li concentration but smaller size than coexisting olivines. In addition, the Li concentration of these clinopyroxene do not vary in any systematic way with indices of magmatic fractionation (e.g. Zr/Hf, La/Sm), but positively correlated with Sr/Y ratio of clinopyroxene which represents the fluid activity (Fig. 5c). These observations indicate that the Li enrichment in clinopyroxene record a recent diffusive ingress of Li into clinopyroxene grain from the hydrous silicate melt. Previous studies have revealed that silicate metasomatism causes preferential Li enrichment in clinopyroxene, whereas carbonatite metasomatism preferentially enriches olivine with same (Seitz and Woodland, 2000; Woodland et al., 2004; Ottolini et al., 2009; Su et al., 2012, 2014, 2017; Gu et al., 2016). Isotopically, carbonatite-metasomatized olivine grains display lower δ^7Li value than normal mantle value and silicate-metasomatized olivine (Su et al., 2014, 2017). Most olivine grains in the Niutoushan, Mingxi and Xilong peridotites have higher Fo content and Li contents, lighter δ^7Li value than what is commonly observed in mantle xenoliths. Their Li concentrations and δ^7Li values mostly plot within the field of carbonatite metasomatism (Figs. 2 and 5d), recording the earlier carbonatite metasomatism occurred before hydrous silicate metasomatism (Figs. 2 and 5d). Previous studies have reported that progressive dehydration in the subduction zone through preferential loss of isotopically heavy Li into fluid phase could induce low δ^7Li residual slab, as observed in eclogite (δ^7Li down to −22‰; Wunder et al., 2006; Xiao et al., 2011), which may be the origin of low δ^7Li metasomatic melts. In addition, the subduction-related melt/fluid produced by dehydration processes most likely metasomatized the depleted mantle domain with elevated fluid-mobile element contents (e.g., Li, Sr, Th, U, La, and Pb; Deng et al., 2017), consistent with the trace element of clinopyroxene in this study. Specially, the Niutoushan, Mingxi and Xilong peridotites display deleted Sr and Nd isotopic compositions (Xu et al., 2003). Since the Cathaysia block has been an active continental margin since the mid-Permian (Li and Li, 2007), the metasomatic agent involved in the metasomatism of lithospheric mantle beneath the Cathaysia block may be derived from a highly dehydrated slab.

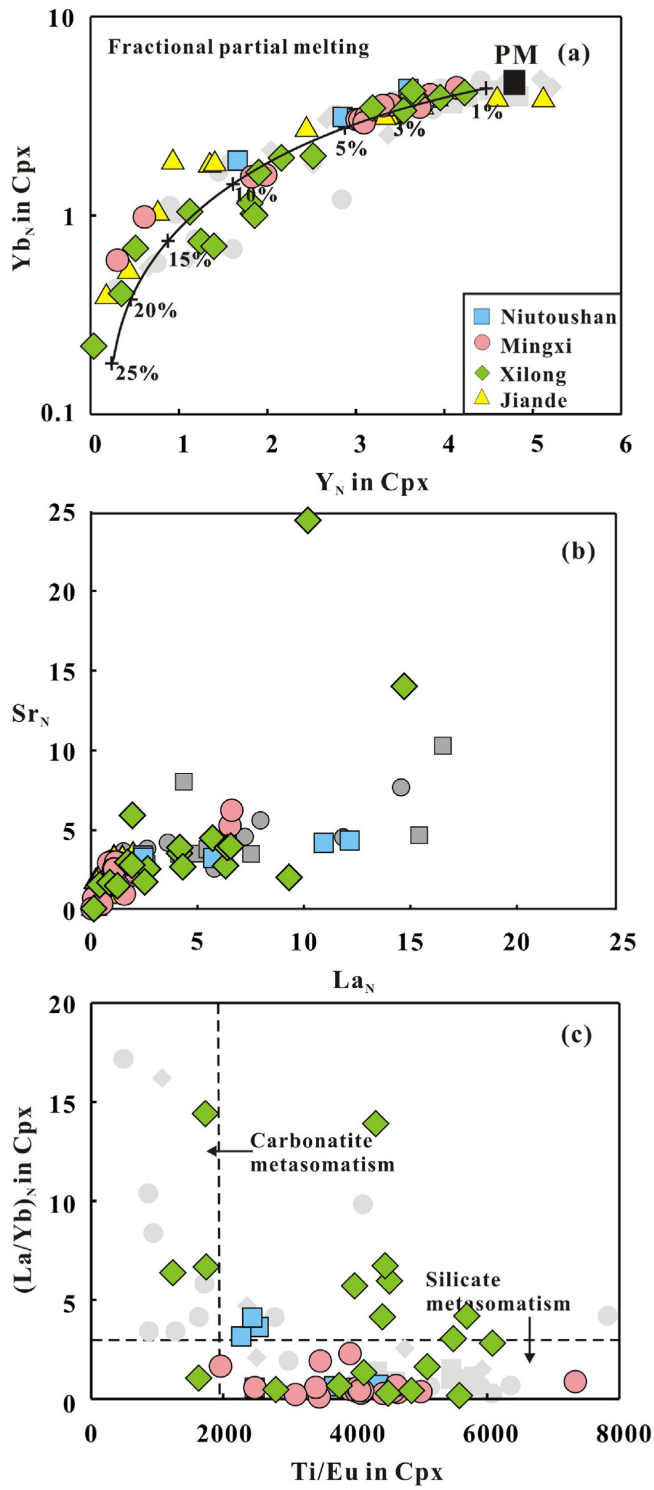

Fig. 4. (a) Fractional melting model based on Y_N vs. Yb_N in primary clinopyroxene (modified from Norman, 1998) within the spinel stability field. (b) La_N vs. Sr_N in primary clinopyroxene from the Niutoushan, Mingxi and Xilong peridotites. (c) $(La/Yb)_N$ vs. Ti/Eu in primary clinopyroxene from the Niutoushan, Mingxi and Xilong peridotites. The subscript N indicates normalization to the primitive mantle compositions of McDonough and Sun (1995). Grey symbols represent the Niutoushan, Mingxi, and Xilong peridotites in the literature (Xu et al., 2000, 2003; Yu et al., 2011; Lu et al., 2015; Liu et al., 2017). Jiande peridotite data shown for comparison are from Hao et al. (2014) and Xiao et al. (2017). Signatures of silicate metasomatism and carbonatite metasomatism in Fig. 4c are from Coltorti et al. (1999).

5.3. Implications for mantle heterogeneity beneath the Cathaysia block

The stagnation of the Pacific plate within the mantle transition zone is revealed through global seismic tomography beneath the eastern Asia (Chen and Ai, 2009; Zhao et al., 2009, 2017), which could transport huge amount of sediments, oceanic crust and lithosphere into the upper mantle. The decarbonization and dehydration of the stagnant slab would release H_2O and CO_2 into the overlying upper mantle, resulting in the chemical heterogeneity of the mantle wedge, as evidenced by the late Cretaceous-Cenozoic basalts in eastern Asia (Xu et al., 2018). On the other hand, the carbonatite inclusions in peridotite xenoliths captured by Cenozoic basalts from Shandong indicate that carbonatite metasomatism is not only confined to the asthenosphere, but also extend to the shallow lithospheric mantle (Deng et al., 2017).

Many elements have been developed as tracers for recycled components. For instance, Li and Ba enrichment in basalts commonly indicate the presence of subduction components in their source regions (Elliott, 2003; Pearce et al., 2005). In South China, there are trends of increasing Li and Ba contents along with increasing distance from the present subduction trench for the Cenozoic basalts (Fig. 1e and f; Huang et al., 2017; Su et al., 2017). Furthermore, these basalts have low δ^{26}Mg values and also display a decreasing δ^{26}Mg value trend with increasing distance from the present subduction trench (Huang et al., 2015; Su et al., 2017). These features are considered to be related to the subduction of Pacific oceanic plate (Huang et al., 2015, 2017; Su et al., 2017). In the Niutoushan, Mingxi and Xilong peridotites, the Li systematics of olivine and clinopyroxene trace element data also recorded two episodes of metasomatism after variable degrees of melt extraction (Figs. 2, 3 and 5). Moreover, the Niutoushan lherzolites which are more southerly locality, have experienced less carbonatite metasomatism relative to Mingxi and Xilong peridotites. From Niutoushan, Mingxi to Xilong peridotites, the Li concentration of olivine and clinopyroxene increases with increasing distance from the present subduction trench for the peridotites, which is consistent with those of basalts in South China (Fig. 1b and c). The metasomatic melt/fluid may have resulted from dehydration processes via the westward subduction of the Paleo-Pacific slab. However, the Jiande lherzolite which is the most distantly located from the trench shows ‘mantle-like’ Li features. Xiao et al. (2017) revealed that Jiande peridotites experienced variable degrees of partial melting but little imprint from subsequent incipient metasomatism as evidenced by major, trace elemental and Li isotopic composition. In fact, the convective circulation in the mantle wedge and the deep dehydration reactions of the subducting slab may induce asthenosphere upwelling. Thus, Jiande peridotites probably represent upwelling asthenosphere material accreted to the continent. These multiple metasomatisms could have played an important role in changing the chemical composition of lithospheric mantle beneath the Cathaysia block (Xu et al., 1998, 2000, 2003; Yu et al., 2003, 2011; Zheng et al., 2004; Liu et al., 2012, 2017; Lu et al., 2015).

6. Conclusions

Li elemental and isotopic compositions in olivine and clinopyroxene of the Niutoushan, Mingxi, Xilong and Jiande mantle xenoliths indicate disequilibrium Li distributions and heterogeneous Li isotopic compositions beneath the Cathaysia block. The Li systematics, together with major and trace elements, reveal that these peridotites have undergone two stages of metasomatism after variable degrees of partial melting. Clinopyroxene has high Li concentrations and common addition of Th, Sr, and LREE, resulting from a recent diffusive ingress of Li from silicate melts. During the second stage, these peridotites are metasomatized by carbonatitic melts which could have been derived from a highly dehydrated slab as evidenced by extremely low δ^7Li values of olivine. Consequently, these multiple stages of metasomatism related to the subduction of the Pacific oceanic plate resulted in the heterogeneity of lithospheric mantle beneath the Cathaysia block.

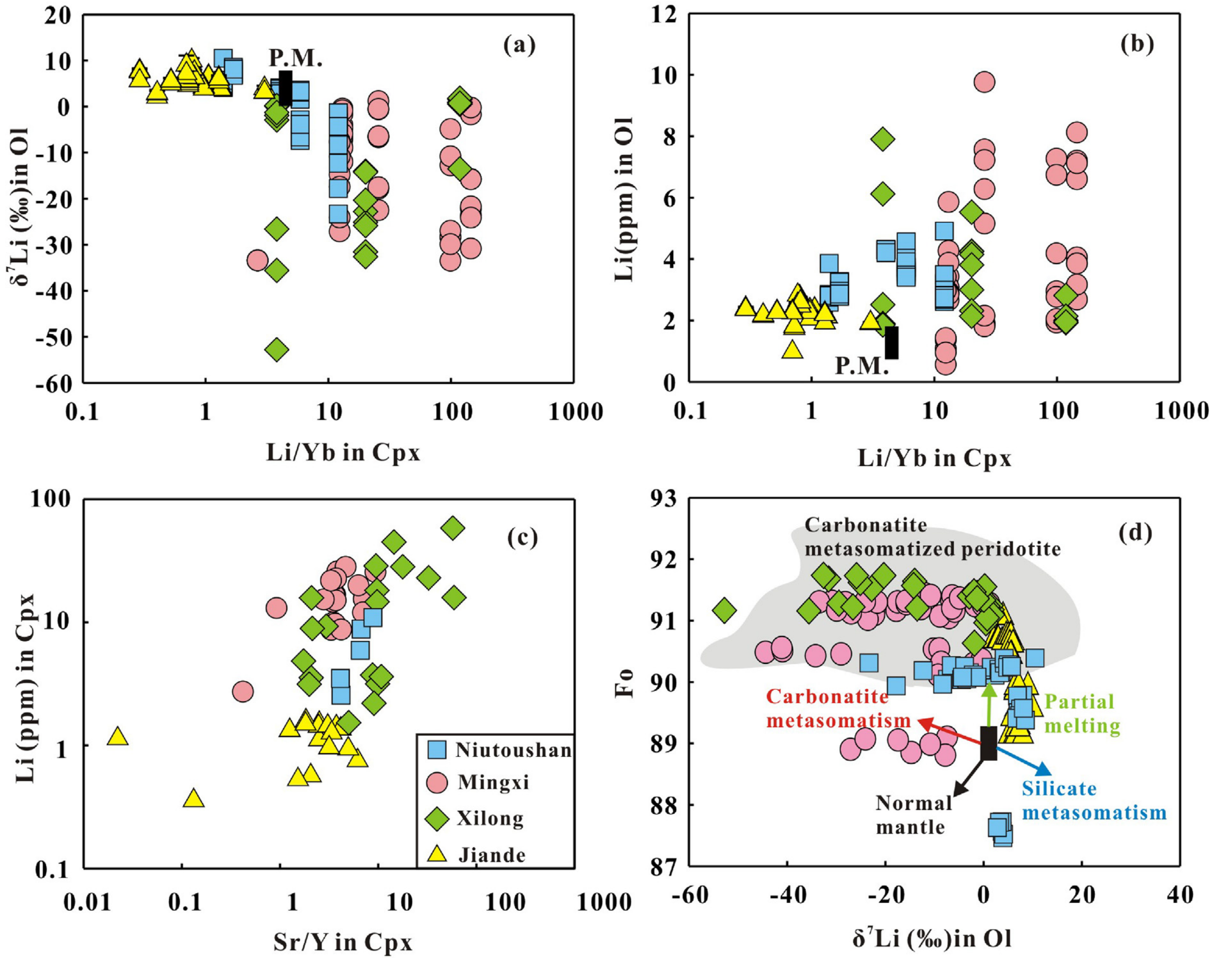

Fig. 5. Correlation diagrams of Li concentration (a) and δ^7Li value (b) of olivine with Li/Yb ratio of clinopyroxene in the Niutoushan, Mingxi, Xilong and Jiande peridotites from the Cathaysia Block. Variation of Li concentration with Sr/Y in primary clinopyroxene from the Niutoushan, Mingxi, Xilong and Jiande peridotites (c). Variation of the Fo content with δ^7Li value in the olivine from the Niutoushan, Mingxi, Xilong and Jiande peridotites (d). Jiande peridotite data shown for comparison are from Xiao et al. (2017). The Li concentration of olivine and pyroxene in the upper mantle are from Seitz and Woodland (2000). The Li/Yb ratio of upper mantle is from Jagoutz et al. (1979). Grey field in the Fig. 6c represent the carbanatite metasomatized peridotites in the literature (Su et al., 2019).

Declaration of Competing Interest

The authors declare that they have no known competing financial interests or personal relationships that could have appeared to influence the work reported in this paper.

Acknowledgments

We are grateful to Guo-Qiang Tang, Xiao-Xiao Ling and Jiao Li for helping with the SIMS analyses, Di Zhang and Qian Mao for their assistance with the electron microprobe analyses, and Peng-Fei Zhang, Chen Chen, Jie-Jun Jing and Yang Bai for their important discussions. Constructive and detailed comments from two anonymous reviewers and the editor are greatly appreciated. This study was supported by the National Natural Science Foundation of China (Grants 41673037 and 41688103) and Youth Innovation Promotion Association, Chinese Academy of Sciences (Grant 2017095).

References

Agostini, S., Ryan, J.G., Tonarini, S., Innocenti, F., 2008. Drying and dying of a subducted slab: coupled Li and B isotope variations in Western Anatolia Cenozoic Volcanism. Earth Planet. Sci. Lett. 272, 139–147.

Aulbach, S., Rudnick, R.L., 2009. Origins of non-equilibrium lithium isotopic fractionation in xenolithic peridotite minerals: examples from Tanzania. Chem. Geol. 258, 17–27.

Aulbach, S., Rudnick, R.L., McDonough, W.F., 2008. Li-Sr-Nd Isotope signatures of the plume and cratonic lithospheric mantle beneath the margin of the rifted Tanzanian Craton (Labait). Contrib. Miner. Petrol. 155, 79–92.

Carlson, R.W., Pearson, D.G., James, D.E., 2005. Physical, chemical, and chronological characteristics of continental mantle. Rev. Geophys. 43, RG1001.

Benton, L.D., Ryan, J.G., Savov, I.P., 2004. Lithium abundance and isotope systematics of forearc serpentinites, Conical Seamount, Mariana forearc: insights into the mechanics of slab-mantle exchange during subduction. Geochem. Geophys. Geosyst. https://doi.org/10.1029/2004GC000708.

Chan, L.H., Edmond, J.M., 1988. Variation of lithium isotope composition in the marine environment: a preliminary report. Geochim. Cosmochim. Acta 52, 1711–1717.

Chan, L.H., Edmond, J.M., Thompson, G., Gillis, K., 1992. Lithium isotopic composition of submarine basalts: implication for the lithium cycle in the oceans. Earth Planet. Sci. Lett. 108, 151–160.

Chen, L., Ai, Y.S., 2009. Discontinuity structure of the mantle transition zone beneath the North China Craton from receiver function migration. J. Geophys. Res.-Solid Earth B6.

Coogan, L.A., Kasemann, S.A., Chakraborty, S., 2005. Rates of hydrothermal cooling of new oceanic upper crust derived from lithium-geospeedometry. Earth Planet. Sci. Lett. 240, 415–424.

Coltorti, M., Bonadiman, C., Hinton, R.W., Siena, F., Upton, B.G.J., 1999. Carbonatite metasomatism of the oceanic upper mantle: evidence from clinopyroxenes and glasses in ultramafic xenoliths of Grande Comore, Indian Ocean. J. Petrol. 40, 133–165.

Deng, L., Liu, Y.S., Zong, K.Q., Zhu, L.Y., Xu, R., Hu, Z.C., Gao, S., 2017. Trace element and Sr isotope records of multi-episode carbonatite metasomatism on the eastern margin of the North China Craton. Geochem. Geophys. Geosyst. 18, 220–237.

Dohmen, R., Kasemann, S.A., Coogan, L., Chakraborty, S., 2010. Diffusion of Li in olivine. Part I: experimental observations and a multi species diffusion model. Geochim. Cosmochim. Acta 74, 274–292.

Downes, H., 2001. Formation and modification of the shallow sub-continental lithospheric mantle: a review of geochemical evidence from ultramafic xenoliths suites

and tectonically emplaced ultramafic massifs of western and central Europe. J. Petrol. 42, 233–250.
Elliott, T., 2003. Tracers of the slab. In: In: Eiler, J.M. (Ed.), Inside the Subduction Factory. Geophysical Monograph Series, vol. 138. American Geophysical Union, Washington, DC, pp. 23–45.
Fan, Q.C., Hooper, P.R., 1989. The mineral chemistry of ultramafic xenoliths of eastern China: implications for upper mantle composition and the paleogeotherms. J. Petrol. 30, 1117–1158.
Fan, Q.C., Hooper, P.R., 1991. The Cenozoic basaltic rocks of eastern China: petrology and chemical composition. J. Petrol. 32, 765–810.
Fan, W.M., Menzies, M.A., 1992. Destruction of aged lower lithosphere and acceretion of asthenosphere mantle beneath eastern China. Geotectonica et Metallogenia 16, 171–180.
Fan, W.M., Zhang, H.F., Baker, J., Jarvis, K.E., Mason, P.R.D., Menzies, M.A., 2000. On and off the North China craton: where is the Archean keel? J. Petrol. 41, 933–950.
Gao, Y., Snow, J.E., Casey, J.F., Yu, J., 2011. Cooling-induced fractionation of mantle Li isotopes from the ultraslow-spreading Gakkel Ridge. Earth Planet. Sci. Lett. 301, 231–240.
Griffin, W.L., Zhang, A., O'Reilly, S.Y., Ryan, C.G., 1998. Phanerozoic evolution of the lithosphere beneath the Sino-Korean craton. In: In: Flower, M., Chung, S.L., Lo, C.H., Lee, Y.Y. (Eds.), Mantle Dynamics and Plate Interactions in East Asia. Geodynamics Series, vol. 27. pp. 107–126.
Gu, X.Y., Deloule, E., France, L., Ingrin, J., 2016. Multi-stage metasomatism revealed by trace element and Li isotope distributions in minerals of peridotite xenoliths from Allègre volcano (French Massif Central). Lithos 264, 158–174.
Halama, R., Savov, I.P., Rudnick, R.L., McDonough, W.F., 2009. Insights into Li and Li isotope cycling and sub-arc metasomatism from veined mantle xenoliths, Kamchatka. Contrib. Miner. Petrol. 158, 197–222.
Hao, Y.T., Xia, Q.K., Li, Q.W., Chen, H., Feng, M., 2014. Partial melting control of water contents in the Cenozoic lithospheric mantle of the Cathaysia block of South China. Chem. Geol. 380, 7–19.
Ho, K.S., Chen, J.C., Lo, C.H., Zhao, H.L., 2003. ^{40}Ar-^{39}Ar dating and geochemical characteristics of late Cenozoic basaltic rocks from the Zhejiang-Fujian region, SE China: eruption ages, magma evolution and petrogenesis. Chem. Geol. 197, 287–318.
Huang, J., Li, S.G., Xiao, Y.L., Ke, S., Li, W.Y., Tian, Y., 2015. Origin of low δ^{26}Mg Cenozoic basalts from South China Block and their geodynamic implications. Geochim. Cosmochim. Acta 164, 298–317.
Huang, X.L., Xu, Y.G., 2010. Thermal state and structure of the lithosphere beneath eastern China: a synthesis on basalt-borne xenoliths. J. Earth Sci. 21, 711–730.
Huang, X.W., Su, B.X., Zhou, M.F., Gao, J.F., Qi, L., 2017. Cenozoic basalts in SE China: chalcophile element geochemistry, sulfide saturation history, and source heterogeneity. Lithos 282, 215–227.
Ionov, D.A., Seitz, H.M., 2008. Lithium abundances and isotopic compositions in mantle xenoliths from subduction and intra-plate settings: mantle sources vs. eruption histories. Earth Planet. Sci. Lett. 266, 316–331.
Jagoutz, E., Palme, H., Baddenhausen, H., Blum, K., Cendales, M., Dreibus, G., Spettel, B., Lorenz, V., Wänke, H., 1979. The abundances of major, minor and trace elements in the earth's mantle as derived from primitive ultramafic nodules. In: Lunar Planetary Science Conference 10th, pp. 2031–2050.
Jeffcoate, A.B., Elliott, T., Kasemann, S.A., Ionov, D., Cooper, K.M., 2007. Li isotope fractionation in peridotites and mafic melts. Geochim. Cosmochim. Acta 71, 202–218.
Lai, Y.J., Pogge von Strandmann, P.A.E., Dohmen, R., Takazawa, E., Elliott, E., 2015. The influence of melt infiltration on the Li and Mg isotopic composition of the Horoman Peridotite Massif. Geochim. Cosmochim. Acta 164, 318–332.
Li, S.G., Xiao, Y.L., Liou, D.L., Chen, Y.Z., Ge, N.J., Zhang, Z.Q., Sun, S.S., Cong, B.L., Zhang, R.Y., Hart, S.R., 1993. Collision of the North China and Yangtse Blocks and formation of coesite-bearing eclogites: timing and processes. Chem. Geol. 109, 89–111.
Li, Z.X., Li, X.H., 2007. Formation of the 1300-km-wide intracontinenal orogen and postorogenic magmatic province in Mesozoic South China: a flat-slab subduction model. Geology 35, 179–182.
Liu, C.Z., Wu, F.Y., Sun, J., Chu, Z.Y., Qiu, Z.L., 2012. The Xinchang peridotite xenoliths reveal mantle replacement in southeastern China. Lithos 150, 171–187.
Liu, C.Z., Zhang, C., Liu, Z.C., Sun, J., Chu, Z.Y., Qiu, Z.L., 2017. Formation age and metasomatism of the sub-continental lithospheric mantle beneath southeast China: Sr-Nd-Hf-Os isotopes of Mingxi mantle xenoliths. J. Asian Earth Sci. 145, 591–604.
Liu, R., Zhou, H.W., Zhang, L., Zhong, Z.Q., Zeng, W., Xiang, H., Song, J., Lu, X.Q., Li, C.Z., 2009. Paleoproterozoic reworking of ancient crust in the Cathaysia Block, South China: evidence from zircon trace elements, U-Pb and Lu-Hf isotopes. Chin. Sci. Bull. 54, 1543–1554.
Liu, S.C., Xia, Q.K., Choi, S.H., Deloule, E., Li, P., 2016. Continuous supply of recycled Pacific oceanic materials in the source of Cenozoic basalts in SE China: the Zhejiang case. Contrib. Miner. Petrol. 171, 100.
Lu, J.G., Zheng, J.P., Griffin, W.L., O'Reilly, S.Y., Pearson, N.J., 2015. Microscale effects of melt infiltration into the lithospheric mantle: peridotite xenoliths from Xilong, South China. Lithos 232, 111–123.
Magna, T., Ionov, D.A., Oberli, F., Wiechert, U., 2008. Links between mantle metasomatism and lithium isotopes: evidence from glass-bearing and cryptically metasomatized xenoliths from Mongolia. Earth Planet. Sci. Lett. 276, 214–222.
Magna, T., Wiechert, U., Grove, T.L., Halliday, A.N., 2006. Lithium isotope fractionation in the Southern Cascadia subduction zone. Earth Planet. Sci. Lett. 250, 428–443.
Marschall, H.R., Pogge von Strandmann, P.A.E., Seitz, H.M., Elliott, T., Niu, Y., 2007. The lithium isotopic composition of orogenic eclogites and deep subducted slabs. Earth Planet. Sci. Lett. 262, 563–580.
McDonough, W.F., Sun, S.S., 1995. The composition of the Earth. Chem. Geol. 120, 223–253.
Menzies, M.A., Fan, W., Zhang, M., 1993. Palaeozoic and Cenozoic lithoprobes and loss of > 120 km of Archaean lithosphere, Sino-Korean craton, China. In: Magmatic Processes and Plate Tectonics. Geological Society Special Publication, pp. 71–81.
Menzies, M.A., Xu, Y.G., 1998. Geodynamics of the North China Craton. In: Flower, M.F.J., Chung, S.L., Lo, C.H., Lee, T.Y. (Eds.), Mantle Dynamics and Plate Interactions in East Asia. American Geophysical Union, Washington D.C., pp. 155–165.
Moriguti, T., Nakamura, E., 1998. Across-arc variation of Li isotopes in lavas and implication for crust/mantle recycling at subduction zones, Earth Planet. Sci. Lett. 163, 167–174.
Navon, O., Stolper, E., 1987. Geochemical consequences of melt percolation: the upper mantle as a chromatographic column. J. Geol. 95, 285–307.
Norman, M.D., 1998. Melting and metasomatism in the continental lithosphere: laser ablation ICPMS analysis of minerals in spinel lherzolites from eastern Australia. Contrib. Miner. Petrol. 130, 240–255.
Ottolini, L., Laporte, D., Raffone, N., Devidal, J.L., Le Fevre, B., 2009. New experimental determination of Li and B partition coefficients during upper mantle partial melting. Contrib. Miner. Petrol. 157, 313–325.
O'Reilly, S.Y., Griffin, W.L., 1988. Mantle metasomatism beneath Victoria, Australia: I. Metasomatic processes in Cr-diopside lherzolites. Geochim. Cosmochim. Acta 52, 433–447.
O'Reilly, S.Y., Griffin, W.L., Poudjom, Y.H., Morgan, P., 2001. Are lithospheres forever? Tracking changes in subcontinental lithospheric mantle through time. GSA Today 11, 4–10.
O'Reilly, S.Y., Griffin, W.L., Ryan, C.G., 1991. Residence of trace elements in metasomatized spinel lherzolite xenoliths: a protonmicroprobe study. Contrib. Miner. Petrol. 109, 98–113.
Pearce, J.A., Stern, R.J., Bloomer, S.H., Fryer, P., 2005. Geochemical mapping of the Mariana arc-basin system: implications for the nature and distribution of subduction components. Geochem. Geophys. Geosyst. https://doi.org/10.1029/2004GC000895.
Parkinson, I.J., Hammond, S.J., James, R.H., Rogers, N.W., 2007. High-temperature lithium isotope fractionation: insights from lithium isotope diffusion in magmatic systems. Earth Planet. Sci. Lett. 257, 609–621.
Pogge von Strandmann, P.A.E., Elliott, T., Marschall, H.R., Coath, C., Lai, Y.J., Jeffcoate, A.B., Ionov, D.A., 2011. Variations of Li and Mg isotope ratios in bulk chondrites and mantle xenoliths. Geochim. Cosmochim. Acta 75, 5247–5268.
Qi, Q., Taylor, L.A., Zhou, X.M., 1995. Petrology and geochemistry of mantle peridotite xenoliths from SE China. J. Petrol. 36, 55–79.
Qiu, Y.M., Gao, S., McNaughton, N.J., Groves, D.I., Ling, W., 2000. First evidence of > 3.2 Ga continental crust in the Yangtze craton of south China and its implications for Archean crustal evolution and Phanerozoic tectonics. Geology 28, 11–14.
Rudnick, R.L., McDonough, W.F., Chappell, B.C., 1993. Carbonatite metasomatism in the northern Tanzanian mantle. Earth Planet. Sci. Lett. 114, 463–475.
Rudnick, R.L., Ionov, D.A., 2007. Lithium elemental and isotopic disequilibrium in minerals from peridotite xenoliths from far-east Russia: product of recent melt/fluid–rock reaction. Earth Planet. Sci. Lett. 256, 278–293.
Ryan, J.G., Langmuir, C.H., 1987. The systematics of lithium abundances in young volcanic rocks. Geochim. Cosmochim. Acta 51, 1727–1741.
Schuessler, J.A., Schoenberg, R., Sigmarsson, O., 2009. Iron and lithium isotope systematics of the Hekla volcano, Iceland: evidence for Fe isotope fractionation during magma differentiation. Chem. Geol. 258, 78–91.
Seitz, H.M., Brey, G.P., Lahaye, Y., Durali, S., Weyer, S., 2004. Lithium isotopic signatures of peridotite xenoliths and isotopic fractionation at high temperature between olivine and pyroxenes. Chem. Geol. 212, 163–177.
Seitz, H.M., Woodland, A.B., 2000. The distribution of lithium in peridotitic and pyroxenitic mantle lithologies: an indicator of magmatic and metasomatic processes. Chem. Geol. 166, 47–64.
Sobolev, A.V., Hofmann, A.W., Kuzmin, D.V., Yaxley, G.M., Arndt, N.T., Chung, S.L., Danyushevsky, L.V., Elliott, T., Frey, F.A., Garcia, M.O., Gurenko, A.A., 2007. The amount of recycled crust in sources of mantle-derived melts. Science 316, 412–417.
Su, B.X., Hu, Y., Teng, F.Z., Xiao, Y., Zhou, X.H., Sun, Y., Zhou, M.F., 2017. Magnesium isotope constraints on subduction contribution to Mesozoic and Cenozoic East Asian continental basalts. Chem. Geol. 466, 112–122.
Su, B.X., Gu, X.Y., Deloule, E., Zhang, H.F., Li, Q.L., Li, X.H., Vigier, N., Tang, Y.J., Tang, G.Q., Liu, Y., Pang, K.N., Brewer, A., Mao, Q., Ma, Y.G., 2015. Potential orthopyroxene, clinopyroxene and olivine reference materials for In-situ lithium isotope determination. Geostand. Geoanal. Res. 39, 357–369.
Su, B.X., Zhang, H.F., Deloule, E., Asamoah, Sakyi P., Xiao, Y., Tang, Y.J., Hu, Y., Ying, J.F., Liu, P.P., 2012. Extremely high and low δ^7Li signatures in the lithospheric mantle. Chem. Geol. 292–293, 149–157.
Su, B.X., Zhang, H.F., Deloule, E., Vigier, N., Hu, Y., Tang, Y.J., Xiao, Y., Sakyi, P.A., 2014. Distinguishing silicate and carbonatite mantle metasomatism by using lithium and its isotopes. Chem. Geol. 381, 67–77.
Su, B.X., Zhou, X.H., Sun, Y., Ying, J.F., Sakyi, P.A., 2018. Carbonatite-metasomatism signature hidden in silicate-metasomatized mantle xenoliths from NE China: insight from Li isotopes. Geol. J. 53, 682–691.
Su, B.X., Hu, Y., Teng, F.Z., Xiao, Y., Zhang, H.F., Sun, Y., Bai, Y., Zhu, B., Zhou, X.H., Ying, J.F., 2019. Light Mg isotopes in mantle-derived lavas caused by chromite crystallization, instead of carbonatite metasomatism. Earth Planet. Sci. Lett. 522, 79–86.
Tang, Y.J., Zhang, H.F., Nakamura, E., Moriguti, T., Kobayashi, K., Ying, J.F., 2007. Lithium isotopic systematics of peridotite xenoliths from Hannuoba, North China Craton: implication for peridotite-melt interaction. Geochim. Cosmochim. Acta 71, 4327–4341.
Tang, Y.J., Zhang, H.F., Nakamura, E., Ying, J.F., 2011. Multistage melt/fluid-peridotite interactions in the refertilized lithospheric mantle beneath the North China Craton:

constraints fromthe Li-Sr-Nd isotopic disequilibrium between minerals of peridotite xenoliths. Contrib. Miner. Petrol. 161, 845–861.
Teng, F.Z., Rudnick, R.L., McDonough, W.F., Gao, S., Tomascak, P.B., Liu, Y., 2008. Lithium isotopic composition and concentration of the deep continental crust. Chem. Geol. 255, 47–59.
Tomascak, P.B., Magna, T., Dohmen, R., 2016. Advances in Lithium Isotope Geochemistry. Springer, Berlin.
Tomascak, P.B., Tera, F., Helz, R.T., Walker, R.J., 1999. The absence of lithium isotope fractionation during basalt differentiation: new measurements by multicollector sector ICP-MS. Geochim. Cosmochim. Acta 63, 907–910.
Wagner, C., Deloule, E., 2007. Behaviour of Li and its isotopes during metasomatism of French Massif Central lherzolites. Geochim. Cosmochim. Acta 71, 4279–4296.
Weyer, S., Seitz, H.M., 2012. Coupled lithium- and iron isotope fractionation during magmatic differentiation. Chem. Geol. 294–295, 42–50.
Windley, B.F., Maruyama, S., Xiao, W.J., 2010. Delamination/thinning of sub-continental lithospheric mantle under Eastern China: the role of water and multiple subduction. Am. J. Sci. 310, 1250–1293.
Woodland, A.B., Seitz, H.M., Yaxley, G.M., 2004. Varying behaviour of Li in metasomatised spinel peridotite xenoliths from Western Victoria, Australia. Lithos 75, 55–66.
Wu, F.Y., Lin, J.Q., Wilde, S.A., Zhang, X.O., Yang, J.H., 2005. Nature and significance of the early cretaceous giant igneous event in eastern China. Earth Planet. Sci. Lett. 233, 103–119.
Wunder, B., Meixner, A., Romer, R.L., Heinrich, W., 2006. Temperature dependent isotopic fractionation of lithium between clinopyroxene and high-pressure hydrous fluids. Contrib. Miner. Petrol. 151, 112–120.
Wulff-Pedersen, E., Neumann, E.R., Jensen, B.B., 1996. The upper mantle under La Palma, Canary Island: formation of Si-K-Na rich melt and its importance as a metasomatic agent. Contrib. Mineral. Petrol. 125, 113–139.
Xia, Y., Xu, X.S., Zhu, K.Y., 2012. Paleoproterozoic S- and A-type granites in southwestern Zhejiang: magmatism, metamorphism and implications for the crustal evolution of the Cathaysia basement. Precambr. Res. 216–219, 177–207.
Xiao, W.J., Windley, B.F., Hao, J., Zhai, M.G., 2003. Accretion leading to collision and the Permian Solonker suture, Inner Mongolia, China: termination of the central Asian orogenic belt. Tectonics 22, 1069.
Xiao, Y., Hoefs, J., Hou, Z., Simon, K., Zhang, Z., 2011. Fluid/rock interaction and mass transfer in continental subduction zones: constraints from trace elements and isotopes (Li, B, O, Sr, Nd, Pb) in UHP rocks from the Chinese Continental Scientific Drilling Program, Sulu, East China. Contrib. Miner. Petrol. 162, 797–819.
Xiao, Y., Zhang, H.F., Deloule, E., Su, B.X., Tang, Y.J., Sakyi, P.A., Hu, Y., Ying, J.F., 2015. Large lithium isotopic variations in minerals from peridotite xenoliths from the eastern North China Craton. J. Geol. 123, 79–84.
Xiao, Y., Zhang, H.F., Su, B.X., Zhu, B., Chen, B.B., Chen, C., 2017. Partial melting control of lithium concentrations and isotopes in the Cenozoic lithospheric mantle beneath Jiande area, the Cathaysia block of SE China. Chem. Geol. 466, 750–761.
Xu, X.S., O'Reilly, S.Y., Griffin, W.L., Zhou, X.M., 1998. The nature of the Cenozoic lithosphere beneath Nushan, East Central China. In: In: Flower, M.F.J., Chung, S.L., Lo, C.H., Lee, T.Y. (Eds.), Mantle Dynamics and Plate Interactions in East Asia. American Geophysical Union. Geodynamics Series, vol. 27. pp. 167–196.
Xu, X.S., O'Reilly, S.Y., Griffin, W.L., Zhou, X.M., 2000. Genesis of young lithospheric mantle in SE China. J. Petrol. 41, 111–148.
Xu, X.S., O'Reilly, S.Y., Griffin, W.L., Zhou, X.M., 2003. Enrichment of upper mantle peridotite: petrological, trace element and isotopic evidence in xenoliths from SE China. Chem. Geol. 198, 163–188.
Xu, Y.G., 2001. Thermo-tectonic destruction of the Archean lithospheric keel beneath the Sino-Korean Craton in China: evidence, timing and mechanism. Phys. Chem. Earth (A) 26, 747–757.
Xu, Y.G., Li, H.Y., Hong, L.B., Ma, L., Ma, Q., Sun, M.D., 2018. Generation of Cenozoic intraplate basalts in the big mantle wedge under eastern Asia. Sci. China Earth Sci. 61, 869–886.
Xu, Z., Zheng, Y.F., 2017. Continental basalts record the crust-mantle interaction in oceanic subduction channel: a geochemical case study from eastern China. J. Asian Earth Sci. 145, 233–259.
Yang, J.H., Zhang, M., Wu, F.Y., 2018. Mesozoic decratonization of the North China Craton by lithospheric delamination: evidence from Sr-Nd-Hf-Os isotopes of mantle xenoliths of Cenozoic alkaline basalts in Yangyuan, Hebei Province, China. J. Asian Earth Sci. 160, 396–407.
Yaxley, G.M., Green, D.H., Kamenetsky, V., 1998. Carbonatite metasomatism in the southeastern Australian lithosphere. J. Petrol. 39, 1917–1930.
Yu, J.H., O'Reilly, S.Y., Griffin, W.L., Xu, X.S., Zhang, M., Zhou, X.M., 2003. The thermal state and composition of the lithospheric mantle beneath the Leizhou Peninsula, South China. J. Volcanol. Geother. Res. 122, 165–189.
Yu, Y., Xu, X.S., Griffin, W.L., O'Reilly, S.Y., Xia, Q.K., 2011. H_2O contents and their modification in the Cenozoic subcontinental lithospheric mantle beneath the Cathaysia block, SE China. Lithos 126, 182–197.
Yu, J.H., O'Reilly, S.Y., Wang, L.J., Griffin, W.L., Zhou, M.F., Zhang, M., Shu, L.S., 2010. Components and episodic growth of Precambrian crust in the Cathaysia Block, South China: evidence from U-Pb ages and Hf isotopes of zircons in Neoproterozoic sediments. Precambr. Res. 181, 97–114.
Zangana, N.A., Downes, H., Thirlwall, M.F., Hegner, E., 1997. Relationship between deformation, equilibration temperatures, REE and radiogenic isotopes in mantle xenoliths (Ray Pic, Massif Central, France): an example of plume-lithosphere interaction? Contrib. Miner. Petrol. 127, 187–203.
Zangana, N.A., Downes, H., Thirlwall, M.F., Marriner, G.F., Bea, F., 1999. Geochemical variation in peridotite xenoliths and their constituent clinopyroxenes from Ray Pic (French Massif Central): implications for the composition of the shallow lithospheric mantle. Chem. Geol. 153, 11–35.
Zhang, H.F., Deloule, E., Tang, Y.J., Ying, J.F., 2010. Melt/rock interaction in remains of refertilized Archean lithospheric mantle in Jiaodong Peninsula, North China Craton: Li isotopic evidence. Contrib. Miner. Petrol. 160, 261–277.
Zhang, H.F., Sun, M., Zhou, X.H., Zhou, M.F., Fan, W.M., Zheng, J.P., 2003. Secular evolution of the lithosphere beneath the eastern North China Craton: evidence from Mesozoic basalts and high-Mg andesites. Geochim. Cosmochim. Acta 67, 4373–4387.
Zhang, M., Hu, P., Niu, Y., Su, S., 2007. Chemical and stable isotopic constraints on the nature and origin of volatiles in the sub-continental lithospheric mantle beneath eastern China. Lithos 96, 55–66.
Zhang, R.Y., Cong, B.L., 1987. Cenozoic volcanic rocks and the ultramafic xenoliths in southeastern China. In: Er, M.L., Zhao, D.S. (Eds.), Cenozoic Basalts and the Deep-Seated Rock Xenoliths in Eastern China. Science Publication House, Beijing, pp. 349–467 (in Chinese with English abstract).
Zhao, D.P., Tian, Y., Lei, J.S., Liu, L., Zheng, S.H., 2009. Seismic image and origin of the Changbai intraplate volcano in East Asia: role of big mantle wedge above the stagnant Pacific slab. Phys. Earth Planet. Inter. 173, 197–206.
Zhao, D.P., Isozaki, Y., Maruyama, S., 2017. Seismic imaging of the Asian orogens and subduction zones. J. Asian Earth Sci. 145, 349–367.
Zheng, J.P., O'Reilly, S.Y., Griffin, W.L., Lu, F.X., Zhang, M., Pearson, N.J., 2001. Relict refractory mantle beneath the eastern North China block: significance for lithosphere evolution. Lithos 57, 43–66.
Zheng, J.P., O'Reilly, S.Y., Griffin, W.L., Zhang, M., Lu, F.X., Liu, G.L., 2004. Nature and evolution of Mesozoic-Cenozoic lithospheric mantle beneath the Cathaysia block, SE China. Lithos 74, 41–65.
Zhou, X.H., Armstrong, R.L., 1982. Cenozoic volcanic rocks of eastern China—secular and geographic trends in chemistry and strontium isotopic composition. Earth Planet. Sci. Lett. 58, 301–329.
Zhu, R.X., Xu, Y.G., Zhu, G., Zhang, H.F., Xia, Q.K., Zheng, T.Y., 2012. Destruction of the North China Craton. Sci. China Earth Sci. 42, 1135–1159 (in Chinese).
Zhu, R.X., Zheng, T.Y., 2009. Destruction geodynamics of the North China Craton and its Paleoproterozoic plate tectonics. Chin. Sci. Bull. 54, 3354–3366.
Zou, H.B., Zindler, A., Xu, X.S., Qu, Q., 2000. Major, trace element, and Nd, Sr and Pb isotope studies of Cenozoic basalts in SE China: mantle sources, regional variations, and tectonic significance. Chem. Geol. 171, 33–47.